POLITECNICO DI TORINO

Master Degree in Biomedical Engineering

Membrane Electroporation Study by All-atom and Coarse-grained Molecular Dynamics: from Pore Formation to Cell Penetrating Peptide Translocation

Thesis Supervisor

Prof. M. A. Deriu

Co-Supervisors

Prof J. A. Tuszynski
Prof U. Morbiducci

Candidate

Giacomo Nanni

ACADEMIC YEAR 2018/2019

Table of contents

Abstract 5

1 Introduction 6

2 Materials and Methods 8

2.1 Molecular modelling 8
2.2 Molecular Mechanics 8
2.2.1 Potential Energy Function 9
2.2.2 Bonded and Non-bonded interactions 9
2.2.3 Periodic boundary conditions 11
2.2.4 Potential energy minimization 12
2.3 Molecular Dynamics 12
2.3.1 Theoretical background 12
2.3.2 Implementation scheme 14
2.4 Coarse-Grained Approach 16
2.4.1 MARTINI force field 16
2.5 Electric Fields in GROMACS 18

3 Membrane electroporation: poration dynamics 20

3.1 Introduction 20
3.2 Materials and Methods 22
3.2.1 System topologies and coordinates in AA simulations 22
3.2.2 Simulation setup in AA simulations 23
3.2.3 System topologies and coordinates in CG simulations 24
3.2.4 Simulation setup in CG simulations 25
3.2.5 Electroporation 26
3.3 Results 28
3.3.1 AA simulations 28
3.3.2 CG simulations 30
3.4 Discussion 33
3.5 Conclusions 35

4 CPP direct penetration through water pores driven by ionic imbalance in coarse-grained simulations 36

4.1 Introduction **36**
4.2 Materials and methods **39**
4.2.1 System coordinates and topologies 39
4.2.2 Cell penetrating peptides (CPP) 40
4.2.3 Water pore formation 42
4.2.4 Simulation setup 43
4.3 Results **44**
4.3.1 Water pore formation 44
4.3.2 CPPs penetration mechanism 47
4.4 Discussion **51**
4.5 Conclusions **52**

5 References **53**

6 SUPPORTING INFORMATION **62**

6.1 Chapter 3-SI **62**
6.1.1 Bilayer area 62

Abstract

Cell membranes fulfil many important biological functions and are composed by a heterogeneous variety of lipids and proteins, which leads to the typical asymmetric bilayer structure. One of the main functions of cell membrane is to act as a filter to control the molecule traffic at the interface. The comprehension of the molecular transport across the membrane is hugely important in medicine, in particular in the development of effective drug delivery system. There are different routes for cellular uptake, some involving complex signalling pathways, some more simple. The easier way is the direct translocation through water pores. Indirect experimental evidences suggest the presence of small, short-lived pores for which today experimental tools are unable to provide direct observation and atomistic detail. Here, through molecular modelling, the formation of these hydrophilic pores was observed and analysed. In particular, the focus was on the effect of the transmembrane potential, which has a strong influence on the transport of various small and large molecules across the membrane and leads to pore formation. In the present work, lipid pores were induced both applying an external, constant electric field and creating a physiological-like charge imbalance across the membrane. Moreover, following the second approach, cellular uptake of seven different cell penetrating peptides (CPPs) through direct translocation pathway driven by the membrane electrostatic potential was observed and studied. The opening of membrane pores due to the ion imbalance revealed to be broadly relevant for CPP uptake.

1 Introduction

The current chapter is devoted to a general introduction of the present Master Thesis work, elucidating aims and objectives.

Plasma membrane represents the physiological barrier that all molecules have to overcome in order to reach the interior of the cell, thus modulating the behaviour in response to various stimuli and signals. Understanding and influencing the cell permeability is a major topic in medicine, nanomedicine and biomedicine in general, since it is a window on targeted drug-delivery in many diseases. Several different complex pathways of internalization exist and have been analysed in literature and some methods to enhance and control the cellular permeability have been developed. Among them, electroporation is probably the most well established and it has been applied in cancer treatment. It consists in the appearance of pores in cellular membrane caused by an electric field. In the last two-three decades, such method gained increasing attention as a mean of introducing drugs, DNA and other bioactive molecule into cells. When a field is applied, the energy for the water to penetrate into the bilayer is reduced, thus leading to pore formation in nano- to microseconds with radii of at most several nanometers. Such small dimensional scales and timescales are seldom or never reachable experimentally. However, since the first simulation study on electroporation, dated back to 2004, atomistic and coarse-grained molecular dynamics simulations shed the light on mechanisms and the sequence of events of pore formation. Simulations pointed out that lipids properties influence the field requested to observe poration events, that the time for pore formation is non-linear with the field applied, that the events at the water-lipid interface are the dominant effect driving the process, just to cite some examples. Thanks to the improvements in electrostatic field modelling and lipid force fields, now the focus of many investigations is moved towards the aim to mimic realistic membrane compositions and in particular the influence of peptides in pore formation mechanism.

The aim of this master thesis is to proceed in that direction, exploiting the transmembrane potential in a real-like membrane to modulate the translocation into cells of cell penetrating peptides, which are short-sequence, non-toxic peptides that have evidenced the ability to

cross the membrane and have been successfully used in drug-delivery systems to guide active cargoes inside the cells.

Molecular dynamics simulations performed confirm the mechanisms of pore formation and show that transmembrane potential can drive cell penetrating peptides penetration through water pores.

The work presented is divided into four chapters, briefly summarized below:

Chapter 1 is the current introductory part.

Chapter 2 provides a general view of Materials and Methods applied in this work. Molecular modelling, molecular mechanics and molecular dynamics method key-aspects and physical bases are introduced. A focus on Martini coarse-grained approach and on electric field application in GROMACS is also furnished.

Chapter 3 provides an insight into pore formation dynamics when an external, constant electric field is applied. Different values of the field are investigated both in all-atom and coarse-grained simulations, showing the same poration process in comparable time-scales.

Chapter 4 yields a description of the translocation process of seven cell penetrating peptides across the membrane under the influence of a transmembrane potential that mimics hyperpolarized conditions. Computational results show the ability to modulate the penetration process through a transmembrane potential and emphasize the importance of peptidic charge and sequence, even though the process is more complex and cannot be explained merely accounting for electrostatics.

2 Materials and Methods

This chapter deals with an overview of the theoretical background and the key-aspects of Molecular Dynamics.

2.1 Molecular modelling

Molecular Modelling involves many methods, both theoretical and computational, that provides insight into molecular systems at atomic level, ranging from small compounds to large biological molecules and materials assemblies, by solving the equations of quantum and classical physics to understand and derive macroscopic properties. Today, molecular modelling is associated with computer modelling as the computational techniques have revolutionised this field[1] and drive its increasing use. In fact, thanks to computational improvements, simulations of molecular systems have become much more powerful and accessible over the past few years[2]. Ideally, the relativistic time-dependent Schrödinger equation describes the properties of molecular systems with high accuracy, but anything more complex than the equilibrium state of a few atoms cannot be handled at this ab initio level[3]. Molecular systems, and in particular biological systems, consist of huge number of molecules, thus making impossible the analytical resolution of systems' thermodynamic or kinetic properties. Molecular Dynamics (MD) represents the numerical solution to this challenge, allowing the understanding of molecular processes such as protein conformational changes, ligand binding, multiscale modelling, transport of molecules, membrane properties and much more. In the more simplistic view, MD involves no more than the integration of Newton's equations of motion. MD could be seen as the connection ring between theory and laboratory experiments, as it is able to probe molecular properties that are difficult or impossible to access through wet-lab experiments.

2.2 Molecular Mechanics

Since molecular modelling usually deals with too large systems to be considered by quantum mechanics, Molecular Mechanics (MM) method is used, which implies Newtonian mechanics, calculating the energy of a system as a function of the nuclear positions only, thus ignoring electrons (Born-Oppenheimer approximation). The set of atoms is modelled as interacting through a potential energy function, defined by the molecular force field (FF) used in the

simulation, which is a set of equations that describes the different interactions among the atoms as a function of their positions. The core of MM approach is the set of equations and parameters used to define the FF.

2.2.1 Potential Energy Function

The potential energy function (V) depends on the positions (r) of the N particles composing the systems and is a sum of individual energy contributions:

$$V = V_{bonded} + V_{non-bonded} \tag{2.1}$$

In equation 2.1, the two terms model the interactions between pairs of bonded atoms and the non-bonded interactions between all pairs of atoms that are in different molecules or that are in the same molecule but separated by at least three bonds, respectively. The two terms are given by the following equations 2.2 and 2.3. The bonded interactions take into account energy variations associated to changes in bonds, angles and dihedrals. The non-bonded interactions are given by the summation of van der Waals potential and electrostatic potential. Van der Waals interactions, even though very weak, act on every atom of the system due to the formation of temporary dipoles and are attractive at long range (London dispersion forces) and repulsive at short range (avoiding atom overlapping).

$$V_{bonded} = V_{bonds} + V_{angles} + V_{dihedrals} \tag{2.2}$$

$$V_{non-bonded} = V_{electrostatic} + V_{van\ der\ Waals} \tag{2.3}$$

2.2.2 Bonded and Non-bonded interactions

The terms in equations 2.2 and 2.3 could have different functional forms and different parameters, according to the FF chosen, which usually is the result of a parametrization process, leading to reproduce and predict certain properties. In fact, it is important to

underline that FF are empirical or derived from a quantistic approach. A possible functional form for the potential energy function could be[4]:

$$V(r_1, r_2, \dots, r_N) = \sum_{bonds} \frac{1}{2} k_l [l - l_0]^2 + \sum_{angles} \frac{1}{2} k_\theta [\theta - \theta_0]^2 +$$
$$\sum_{dihedrals} k_\varphi [1 + \cos(n\varphi - \delta)] + \sum_{i=1}^{N} \sum_{j=i+1}^{N} 4\varepsilon_{i,j} \left[\left(\frac{\sigma_{i,j}}{r_{i,j}} \right)^{12} - \left(\frac{\sigma_{i,j}}{r_{i,j}} \right)^{6} \right] + \frac{Q_i Q_j}{4\pi\varepsilon_0 r_{i,j}} \quad (2.4)$$

In equation 2.4, the first term models the interaction between atoms linked by a covalent bond as an harmonic potential, where k_l is the force constant, l_0 is the reference bond length and l is the bond length. The second term, again a harmonic potential, describes the angle between 3 atoms covalently bound, where k_θ is the stiffness and θ_0 the bond angle at the equilibrium. The third term define the dihedral angle among 4 bonded atoms and its energy term is modelled as a series of cosines; k_φ is the energetic barrier related to the angle deformation, δ is the phase that determines the minimum position for the torsional angle and n is the multiplicity. Last two terms define non-bonded interactions, which usually are modelled as functions inversely proportional to the distance between two atoms. The fourth term encompasses the van der Waals potential in the most implemented Lennard-Jones equation, which is defined as the difference between a repulsive term $\left(\frac{\sigma_{i,j}}{r_{i,j}} \right)^{12}$ and an attractive term $\left(\frac{\sigma_{i,j}}{r_{i,j}} \right)^{6}$. It involves $\sigma_{i,j}$ and $r_{i,j}$, which represent the collision diameter (minimum distance with the interaction potential equal to zero) and the depth of the potential well (interaction potential energy minimum), respectively. The last term in equation 2.4 is the electrostatic potential $\frac{Q_i Q_j}{4\pi\varepsilon_0 r_{i,j}}$, which is described by the Coulomb's law with ε_0 free space permittivity, ε_r the relative permittivity and $r_{i,j}$ the distance between the 2 charges Q_i and Q_j. Electrostatic potential decreases only with r so it is considered a long-range interaction. It is worth mentioning that more complex FF could include additional terms.

The greatest amount of computational resources is required by the calculation of the non-bonded interactions, whose number increases as the square of the number of atoms in the system. Thus, several ways were developed to treat the non-bonded interactions cutting off or modifying the non-bonded interactions when atoms are far away from each other. One of

these approaches is the Ewald summation, whose trick was to replace the interaction energies summation in real space with an equivalent summation in Fourier space in the calculation of long-range interactions.

2.2.3 Periodic boundary conditions

In molecular modelling, boundary effect is a crucial issue, since it strongly influences the properties of the whole system, which is composed by few particles. Periodic boundary conditions (PBC) are then used to minimize edge effects in a finite box with a small number of molecules and allow simulating bulk systems. In this way, system has no boundaries and they are replaced by the periodic conditions[5]. The presence of Periodic Boundary Conditions causes imprecisions, but still less severe than the error resulting from artificial boundary with vacuum. Each particle in the box interacts with any other particles in adjacent boxes, which are repeated infinitely. If a particle leaves the box, another comes from the other side (see Figure 1). When long-range interactions are treated through a cutting-off method, to avoid that a particle could see itself in the adjacent box, Minimum Image Convention should be fulfilled by choosing a cut-off distance small enough.

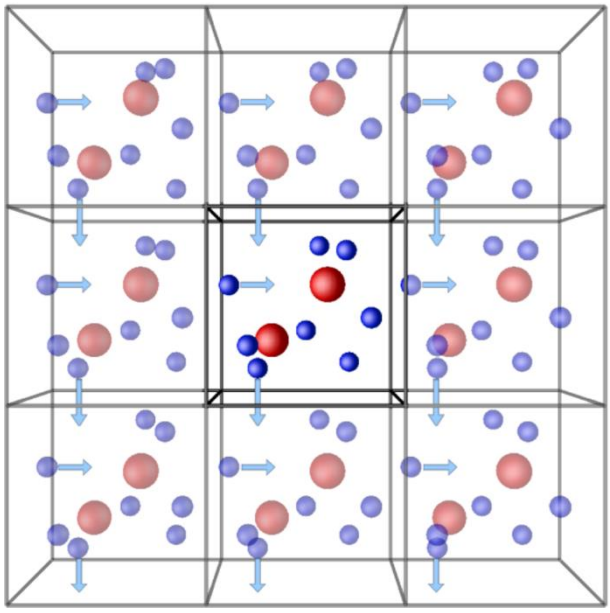

Figure 1.Periodic boundary conditions scheme.

2.2.4 Potential energy minimization

The potential energy function is an extremely complicated, multidimensional function of the coordinates of the system. For a system with N atoms, the potential energy function is a function of 3N Cartesian coordinates. In molecular modelling, the focus in on minimum points on the potential energy surface (PES), which represent the stable state of the system. On the PES there are many local minima and the minimum with the lowest energy is called global minimum. Energy minimization algorithm are used to find those geometries of the systems that correspond to minimum points on PES. Thus, energy minimization leads to a reduction in the potential energy of the system. The ideal minimization algorithm should provide the answer as quickly as possible, using the least amount of memory. Minimization algorithm could be classified into two groups: derivative methods and non-derivative method. Among the derivative methods it is possible to distinguish between first order method (e.g. Steepest Descent, Conjugate Gradient) and second order methods (e.g. Newton-Raphson, L-BFGS). First derivative methods gradually change the coordinates of the atoms, moving towards the energy minimum, starting from the configuration obtained at the previous step. Second derivatives provide information about the curvature of the function by calculating the Hessian matrix.

2.3 Molecular Dynamics

MD is a simulation method that allows generating the trajectory of a molecular system by solving Newton's equations of motion. Therefore, average properties and time-dependent behaviour of the system can be derived.

2.3.1 Theoretical background

Macroscopic physical properties can be distinguished by static equilibrium properties (e.g. average potential energy, radial distribution function) and dynamic or non-equilibrium properties (e.g. dynamics if phase changes, reaction kinetics). Molecular dynamics allows generating both representative equilibrium ensembles and non-equilibrium ensembles. These properties can be computed as ensemble averages over a representative statistical ensemble of molecular systems. Consequently, it is necessary to generate a representative ensemble at a given temperature. The science of statistical mechanics is the theoretical framework for such

calculations[3]. A statistical ensemble is a collection of all possible systems that have different microscopic states but have an identical macroscopic or thermodynamic state. The microscopic state of the system is defined by the atomic positions r and momenta p; these coordinates are in a multidimensional space called phase space. There are different ensembles:

- Micro-canonical Ensemble (NVE); it is characterized by a fixed volume, energy and number of atoms.
- The Canonical Ensemble (NVT); it is characterized by a fixed volume, temperature and number of atoms.
- Isobaric-isothermal ensemble (NPT); with fixed number of particles, pressure and temperature.
- Grand Canonical or Gibbs ensemble (μVT); characterized by a fixed volume, temperature and chemical potential.

In statistical mechanics the ensemble average of a property A is calculated over all possible configurations of the system:

$$\langle A_{ensemble} \rangle = \iint dp^N dr^N A(p^N, r^N) \rho(p^N, r^N) \tag{2.5}$$

In equation 2.5 there should be 6N integral signs on the integral for the 6N positions and momenta for all particles. $\rho(p^N, r^N)$ is the probability density of the ensemble and could be written as a Boltzmann distribution:

$$\rho(p^N, r^N) = \frac{1}{Q} e^{-\frac{E(p^N, r^N)}{k_B T}} \tag{2.6}$$

In equation 2.6 E is the energy, T is the temperature, k_B is the Boltzmann factor, Q is the partition function, expressed by:

$$Q = \iint dp^N dr^N \, e^{-\frac{E(p^N, r^N)}{k_B T}} \tag{2.7}$$

The partition function is a dimensionless normalising sum of Boltzmann factors over all microstates of the system. It is very important because it relates microscopic thermodynamic variables to macroscopic functions of state. However, it is extremely difficult to calculate because one should calculate all possible states of the system and its analytical solution is impossible. Fortunately, it is possible to overcome this issue thanks to the ergodic hypothesis, which allows replacing the ensemble average with the time average over sufficiently long periods:

$$\langle A_{ensemble} \rangle = \langle A_{time} \rangle = \lim_{\tau \to \infty} \frac{1}{\tau} \int_{t=0}^{\tau} A\big(p^N(t), r^N(t)\big) dt \cong \frac{1}{M} \sum_{t=1}^{M} A(p^N, r^N) \tag{2.8}$$

In equation 2.8 t is the simulation time, M is the time-step and $A(p^N, r^N)$ is the instantaneous value of the property A. The idea is that over a long period of time the system will pass through all possible states, and thus it becomes possible to compute ensemble-average properties.

2.3.2 Implementation scheme

MD is a simulation method that solves Newton's equations of motion for a system of N interacting atoms:

$$m_i \frac{\partial^2 r_i}{\partial t^2} = F_i, i = 1, \dots, N \tag{2.9}$$

The forces are the negative derivatives of the potential function V:

$$F_i = -\frac{\partial V}{\partial r_i} \tag{2.10}$$

The potential energy is a complex, continuous function which cannot be solved analytically. Therefore, sets of atomic positions are derived in sequence, in a deterministic way, calculating them numerically time-step by time-step and thus generating a trajectory, which is the combination of positions and velocities for each atom. In this sense, the choice of the integration time-step is very important (usually from 1 to 10 fs) to avoid instability and to

sample correctly the phase space. A greater time-step allows simulating more quickly, but can make the simulation unstable. A good time step should be less than 1/10th the period of the fastest harmonic oscillator present in the system. A simulation generates representative configurations of the system, permitting to obtain accurate values of structural and thermodynamic properties. In fact, after initial changes, the system will usually reach an equilibrium state, that can be interpreted as a statistical ensemble. There are different integration methods, for example the Verlet algorithm, the Leap-frog algorithm, the Velocity Verlet. The typical MD flowchart is described in Figure 2. Starting from the input structure coordinates, usually derived from experimental data (e.g. Protein Data Bank), and from initial velocities randomly generated from a Maxwell-Boltzmann distribution at a given temperature, the potential energy is calculated according to the FF chosen. Afterwards, forces are calculated by numerical integration and new positions and velocities are generated by the algorithm. The cycle goes on for the number of steps required to reach the equilibrium.

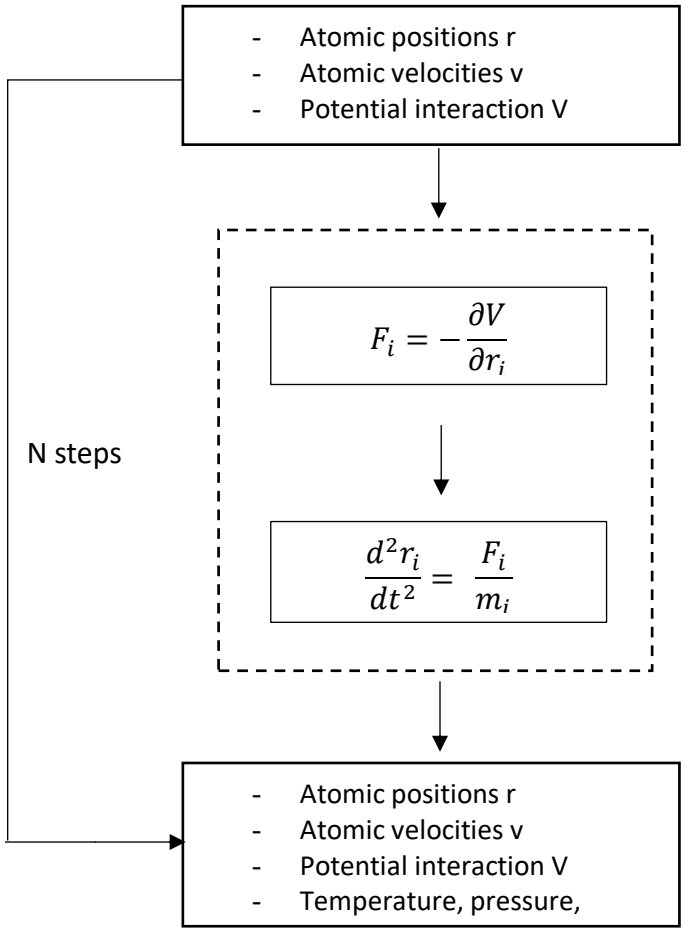

Figure 2. MD typical flowchart: starting from initial position and velocities, new ones are generated, thus leading to the production of a trajectory.

A typical procedure suitable for a MD simulation with a solute molecule in solution consists firstly of an energy minimization step, useful to reduce strong interactions at high energy which could lead to instable simulation. Then, it is performed an equilibration phase (usually hundreds of ps) keeping the solute fixed, in order to reach a desired temperature and/or pressure. Finally, the production run can start. In this phase, thermodynamic properties of the system are calculated, keeping in mind that the system requires many steps to reach a stable state.

2.4 Coarse-Grained Approach

The interesting time scales and system size are often beyond what is attainable by detailed all-atoms MD. Coarse-graining (CG) is a systematic way of reducing the number of degrees of freedom representing a system of interest. To achieve this, typically whole groups of atoms are represented by single beads and the coarse-grained force field describes their effective interactions, removing fine interaction details and losing chemical and spatial resolution. The reduction of the degrees of freedom leads to a smoothed potential energy surface, which allows the use of a longer time step (tens of fs). As well as that, most CG models only compute short-range interactions. Therefore, the simulation dynamics is faster and the phase space sampled is greater. Coarse-grained models are designed to reproduce certain properties of a reference system. This can be either a full atomistic model (bottom-up approach) or even experimental data (top-down approach), in order to reproduce at higher scale level thermodynamic properties. In this case, the generated force field is general such as in the MARTINI approach.

2.4.1 MARTINI force field

Martini, first developed for lipid bilayers[6], has been subsequently expanded to include parameters for proteins and carbohydrates and it is one of the most widely used CG force field (see Figure 3). It is based on a four-to-one mapping of the all atoms model, that is to say on average four heavy atoms plus associated hydrogens are represented by a single interaction centre. Water molecules are involved in this mapping too. Derived from the chemical nature of the underlying structure, CG beads could be assigned a specific particle type with more or less polar character. The four main types of particle are polar (P), non-polar (N), apolar (C) and charged (Q). Within these classes, subtypes are possible and distinguished by a letter

according to the hydrogen-bonding capabilities (d=donor, a=acceptor, da=both, 0=none) or a number indicating the degree of polarity (from 1=low polarity to 5=high polarity). Thus, a total of 18 particle types is possible. Non-bonded interactions were parameterized based on a systematic comparison to experimental thermodynamic data and their potential energy functions are used in a shifted form. For what concerns bonded interactions, they were defined according to structural data derived from the atomistic geometry or obtained from comparison to all-atoms simulations. Generally, Martini simulations are stable with time-steps ranging from 20 to 40 fs.

Focusing on lipids and lipid bilayers, current applications are protein-interplay, characterization of membrane properties, design of drug and gene delivery systems, self-assembly of surfactants, binding and pore-formation in membranes by membrane active peptides.

In particular, three are the major advantages in the use of the Martini over standard all-atoms simulations: (i) allowing many independent simulations in which state conditions are systematically varied; (ii) direct, unbiased sampling of longer time-scales processes becomes possible; (iii) enabling simulations requiring large system sizes.

Obviously, one should keep in mind that Martini, as any other model, has a number of limitations. Some are due to its coarse-grained nature and typical of this approach, others are linked to Martini itself. An interesting issue regards the effective time scale, which in atomistic simulations is well defined and properties such as water diffusion coefficients are used to evaluate the quality of the model. In CG simulations, the modifications in the energy landscape result in a speeding up of the kinetics of the system. This is a key advantage in CG simulations, but the speed-up emerges to be not easy predictable and not the same for all degrees of freedom. Currently, from later diffusion coefficients of lipids, it was pointed out that a semi-universal factor of speed-up is about 4. However, its use has to be considered with care as it is dependent on the type of molecule[7].

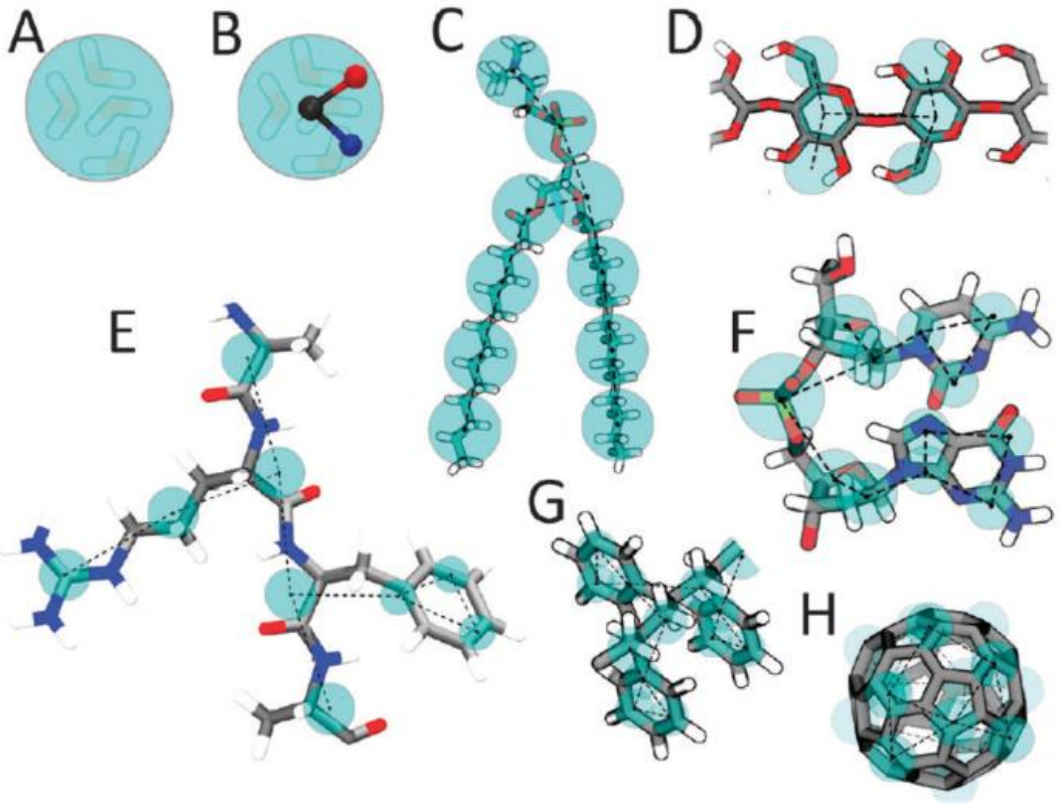

Figure 3. Martini mapping examples of selected molecules. A) Standard water particle representing four water molecules. B) Polarizable water molecule with embedded charges. C) DMPC lipid. D) Polysaccharide fragment. E) Peptide. F) DNA fragment. G) Polystyrene fragment. H) Fullerene molecule. In all cases, Martini CG beads are shown as cyan transparent beads overlaying the atomistic structure.

2.5 Electric Fields in GROMACS

In the present work, GROMACS 5.1.4, GROMACS 2016.3 and 2018.2 software packages were employed to perform simulations. The GROMACS suite, among its several utilities, allows the possibility of applying electric fields across the simulation box. Electric fields are applied when specific options are specified in the GROMACS pre-processor (grompp) input file (.mdp). It is possible to choose between constant field or pulse alternating electric field, which has the form of a Gaussian laser pulse. To apply an electric field in a direction (x, y or z), one should specify three parameters after the appropriate direction. The first parameter is the number of cosines; only 1 with frequency 0 is implemented, so it is always equal to 1. The second parameter sets the strength of the electric field in V/nm. The third parameter defines the phase of the cosine and one can enter any number here since a cosine with a frequency of zero has no phase. For example, the parameters for direction x are set in three fields of E-x (*E*-

x = 1 E_0 0). Concerning the alternating electric field, it can be applied according to equation 2.11:

$$E(t) = E_0 e^{-\frac{(t-t_0)^2}{2\sigma^2}} \cos[\omega(t - t_0)] \tag{2.11}$$

Where E_0 is the field strength, ω the angular frequency, t_0 is the time at of the peak in the field strength and *σ* is the width of the pulse. In such case, the parameters for x-direction are set in the three fields of E-xt (*E-xt* = ω t_0 *σ*).

In GROMACS, an external electric field is introduced in the system as an additional force (qE) acting on all the atoms charged. The effective electric field under periodic boundary conditions is larger than the applied field, depending on the box-size and the dielectric properties of molecules, which have an electric response that varies over time due to induced field generated by local dipoles and dipoles in the surrounding boxes.

During electroporation simulations, the geometry of the membrane changes, with an increase in the bilayer area, thus leading to considerable changes in the field strength. Thereby, due to the combination of the PME method, which is sensitive to the length of the system in the direction perpendicular to membrane surface, of the electric field and the PBC, the field drastically increases after formation of a high-dielectric membrane spanning water-bridge. Moreover, in the simulation box are present species with different dielectric properties: the water phase, high dielectric, and the lipid phase, low dielectric[8–11].

3 Membrane electroporation: poration dynamics

Membrane permeability is a critical issue in medicine, as the plasma membrane is the barrier all molecules must overcome to reach the intracellular space and exert their action. In particular, the interest is on driving bioactive agents inside, such as drugs, targeting specific cells. Electroporation is a method that induces the formation of hydrophilic pores across the membrane by applying electric field. Molecular modelling allows describing with atomic resolution the formation of the hydrophilic pore. In this study, membrane poration driven by the action of electric fields was observed and analysed in all-atom and coarse-grained simulations. It emerged that the poration process is the same and happens in comparable time-scales.

3.1 Introduction

Biological membranes represent complex, self-assembled, heterogeneous structures that are composed by many types of lipids, sterols, proteins, carbohydrates and a number of membrane-associated molecules. Membranes play an active part in numerous functional processes of the life of cells, separating cells and cellular compartments and regulating transport of various molecules, which is fundamental in energy transduction, metabolism and cellular signalling. Lipid molecules can be distinguished by the type of hydrophilic head groups and present a variety of hydrophobic tails. Three classes of amphipathic lipids compose the membrane: phospholipids, glycolipids and sterols. Phospholipids are built of a hydrophilic phosphate group (head) and two hydrophobic fatty acids (tail), all joined together by a glycerol molecule. Glycolipids can contain either glycerol or sphingosine and are characterized by the presence of a sugar in place of the phosphate head group. Cholesterol consists of a hydrophilic hydroxyl group that is the head region, a four-ring steroid structure and a short hydrocarbon side chain. Even though the lipid composition of the plasma membrane in different organisms and cell types varies significantly and depends on the stage of the cell cycle and environmental factors, an average mammalian plasma membrane contains six major phospholipids (phosphatidylcholine, phosphatidylserine, phosphatidylethanolamine, phosphatidylinositol and sphingomyelin) which together constitute 50 to 60% of total membrane lipid. Glycolipids and cholesterol generally correspond to about 40% of the total membrane lipid molecules. Normally, lipids are zwitterionic (neutral) or anionic and are various and distributed

asymmetrically across the membrane in most eukaryotic cells. The heterogeneity in lipids composing membranes suggests the idea that there must be evolutionary advantages that are dependent on a complex lipid repertoire. The outer leaflet of the plasma membrane consists principally of phosphatidylcholine and sphingomyelin, whereas phosphatidylethanolamine and phosphatidylserine are the predominant phospholipids of the inner leaflet. The head groups of both phosphatidylserine and phosphatidylinositol are negatively charged, so their predominance in the inner leaflet results in a net negative charge on the cytosolic face of the plasma membrane. The glycolipids are found exclusively in the outer leaflet of the plasma membrane, with their carbohydrate portions exposed on the cell surface. Physiologically, lipid bilayers commonly exist in fluid state, called liquid disordered state, considering the relatively high degree of disorder[12–15].

In medicine and biotechnology, methods to temporary interrupt the membrane integrity are of huge interest and very attractive, because they enable the transfer of active molecules, such as drugs, genes, antibodies, and thereby permit to modulate processes by modifying the cell interior. In this sense, the most established technique is electroporation and it is based on the application of external electric fields. The action of electrical pulses on a microsecond to millisecond time scale induces the formation of small hydrophilic pores across the membrane, thus allowing the transfer of molecules from outside to inside[16]. Such approach was also developed and applied in the treatment of cancer[17]. A remarkable feature of pore formation is its reversibility under certain conditions (removal of the field, reduction of the field). It has been revealed that electroporation can generate a transmembrane voltage of typically 200 mV-1 V for a typical cell thickness of 5 nm[18]. MD simulations showed that a transverse electric field can produce pores in membranes and revealed the molecular mechanisms and the stages of pore formation with atomistic resolution and at short time scales, not possible experimentally. To mimic a transmembrane potential, two possible approaches can be followed: generating an ion imbalance across the membrane, in a physiological-like manner, or applying an external electric field in direction normal to the membrane. The main problem of both currently used protocols is the creation of unstable pores. In the electric field method, pores grow uncontrolled and lead to rupture of the bilayer, while in the charge imbalance method, the transmembrane potential decreases due to ion flow, which tend to re-balance the gradient, and thus the pore closes. Both methods lead to poration in the same time scales

(tens of nanoseconds). Another drawback of MD simulations concerns the value of the applied field, which is far from being physiological, in order to overcome the large activation energy required to electroporate in a reasonable time window (hundreds of nanoseconds). However, the value of the field reachable in simulations is consistent with the transmembrane voltage used for electroporation in experiments.

Here, the attention is put on the effect that an external electric field has on the poration dynamics in a physiological-mimicking membrane. This is a novelty, because usually, in literature, the focus is on simpler single-component or double-component bilayer systems. In particular, both all-atom and coarse-grained simulations were performed, compared and analysed to give an overview of the pore formation dynamics.

3.2 Materials and Methods

3.2.1 System topologies and coordinates in AA simulations

An asymmetric multi-component membrane (Figure 3.1) was constructed and solvated using CHARMM-GUI[19,20]. Each layer contained 128 lipids and it was composed as in Table 3.1. All major lipids known to reside in mammalian membrane were included with ratios and distribution fitting an idealized real membrane. In the inner leaflet were placed the charged species phosphatidylserine (PS), phosphatidylinositol (PI), phosphatidic acid (PA), phosphatidylinositol (PI) and phosphatidylinositol-1,3-biphosphate (PI13). In the outer leaflet were placed the glycolipids (GM). In both leaflets are present the zwitterionic lipids phosphatidylcholine (PC), sphingomyelin (SM) and phosphatidylethanolamine (PE), with PC and SM principally in the outer layer and PE in the inner one, where lysophosphatidylcholine (LPC) was also included. In all cases, the hydrophobic tails are palmitic acid and oleic acid, saturated and monounsaturated fatty acids respectively. In addition, cholesterol (CHOL) was considered in the model. The system consisted of 69111 particles. The CHARMM36[21] force field was used to define membrane topologies and the TIP3P model was used to describe explicit solvent.

Table 3.1. Membrane composition in AA simulations

	Inner Layer		Outer layer	
Type	**#**	**%**	**#**	**%**
POPC	22	17.2	47	36.7
POPE	33	25.8	7	5.5
PSM	12	9.4	25	19.5
GM1	-	-	3	2.3
GM3	-	-	3	2.3
LPC12	-	-	2	1.6
POPS	14	10.9	-	-
POPI	6	4.7	-	-
POPA	2	1.6	-	-
POPI13	2	1.6	-	-
CHOL	37	28.9	41	32.0
Total	128	100	128	100

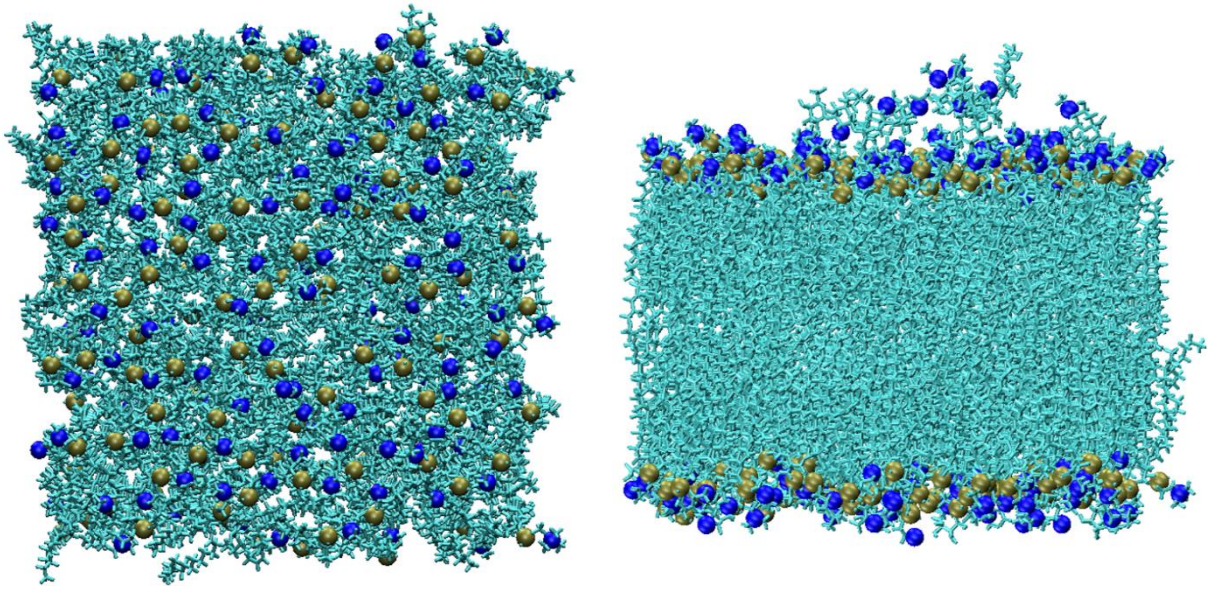

Figure 3.1. Visual inspection of the membrane system. P and N atoms of the headgroups are in tan and blue, respectively. Lipids are in cyan. Top view on the left, side view on the right.

3.2.2 Simulation setup in AA simulations

All-atom molecular dynamics (MD) simulations of asymmetric multi-component membrane systems were conducted under the application of an external electric field perpendicular to membrane's surface.

The system was neutralized by adding counterions. Simulations were performed using the GROMACS 5.1.4[22] and GROMACS 2018.3[22] software packages. First, the system was subject to energy minimization through steepest descent[23] algorithm and then it was undergone to a process of equilibration passing through NVT and NPT runs. During these equilibration runs, Berendsen[24] temperature coupling algorithm and time constant of 1.0 was applied to keep the temperature at 300 K, while Berendsen[24] semiisotropic pressure coupling algorithm with reference pressure equal to 1 bar was employed. All systems were simulated in the NPT ensemble. A 2 fs time step was used. Electrostatic interactions were calculated with the particle-mesh Ewald (PME)[25] method and van der Waals interactions were defined within a cut-off of 1.2 nm. Nose-Hoover[26] and Parrinello-Rahman[27] coupling methods were used as temperature and pressure coupling. Each layer of the membrane and the solvent were coupled separately in temperature. The center-of-mass motion removal was done separately for these three groups too. The LINCS[28] algorithm was used to convert the bonds with hydrogen atoms to constraints. Periodic boundary conditions were applied in all directions.

Five MD replicas of the system with different initial conditions and without the application of an external electric field were run for 150 ns. The final step of one of these equilibrated replicas was taken as starting configuration for electroporation MD simulations. Trajectories were collected every 2 ps and the Visual Molecular Dynamics (VMD)[29] package was employed to display the simulated systems.

3.2.3 System topologies and coordinates in CG simulations

An asymmetric multi-component membrane (Figure 3.2) was constructed and solvated using CHARMM-GUI[19,20]. Each layer contained 100 lipids and it was composed as in Table 3.2. The system consisted of 8838 particles. The martini22p (Martini 2.2 polar amino acids, Martini 2.0 lipids and polarizable water) MARTINI[6,30] force field was used to define lipid and explicit water topologies through a coarse-grained (CG) approach. Differently from the AA membrane-model above, the membrane composition is simpler.

Table 3.2. Membrane composition in CG simulations.

	Inner Layer		Outer Layer	
Type	**#**	**%**	**#**	**%**
POPC	18	18.0	39	39.0
POPE	27	27.0	6	6.0
PSM	10	10.0	21	21.0
POPS	11	11.0	-	-
POPI	5	5.0	-	-
CHOL	29	29.0	34	34.0
Total	100	100	100	100

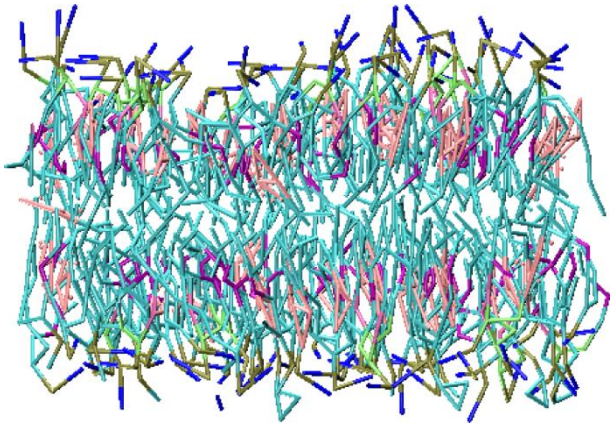

Figure 3.2. Visual inspection of the membrane system used. Lipids in cyan, purple and green; PO4 groups of the headgroups in tan; NC3 groups of the headgroups in blue; cholesterol in pink.

3.2.4 Simulation setup in CG simulations

Coarse-grained molecular dynamics (MD) simulations of asymmetric multi-component membrane systems were conducted under the application of an external electric field perpendicular to membrane's surface.

Simulations were performed using the GROMACS 5.1.4[22] and GROMACS 2016.3[22] software packages. First, each system was subject to energy minimization through steepest descent[23] algorithm and then it was undergone to a process of equilibration passing through three NPT runs with a 2 fs, 10 fs, 20 fs time step respectively. Velocity rescaling[31] temperature coupling

algorithm and time constant of 1.0 ps were applied to keep the temperature at 303.15 K. Berendsen[24] semiisotropic pressure coupling algorithm with reference pressure equal to 1 bar and time constant 5.0 ps was employed. Then, all systems were simulated in the NPT ensemble. A 20 fs time step was used. Electrostatic interactions were calculated with the particle-mesh Ewald (PME)[25] method and van der Waals interactions were defined within a cut-off of 1.2 nm. Velocity rescaling[31] and Parrinello-Rahman[27] coupling methods were used as temperature and semiisotropic pressure coupling, respectively. Time constant was equal to 1 ps for temperature, while it was equal to 12 ps for pressure. The membrane and the solvent were coupled separately in temperature. The center-of-mass motion removal was done separately for these two groups, too. Periodic boundary conditions were applied in all directions. The final step of the equilibration runs was taken as starting configuration for electroporation MD simulations. Trajectories were collected every 10 ps and the Visual Molecular Dynamics (VMD)[29] package was employed to display the simulated systems.

3.2.5 Electroporation

In all-atom simulations, the strength of the electric field was varied from 0.025 V/nm to 1 V/nm. For each value of the field applied, five replicas of the system with different initial conditions were run (see Table 3.3).

Table 3.3. Simulation time for each value of the field in AA simulations.

Field (V/nm)	Simulation time (ns)
0.025	100
0.05	100
0.1	50
0.2	50
0.3	70
0.35	30
0.4	15
0.5	3
1	5

In Martini CG simulations, the strength of the electric field was varied from 0.085 V/nm to 0.5 V/nm. For each value of the field applied, five replicas of the system with different initial conditions were run (see Table 3.4). In addition to the five replicas, a greater membrane was constructed for the case of the 0.2 V/nm field, to test if patch-size has an influence in poration time, as observed elesewhere[10]. This system was built by doubling one of the smaller 100-lipid membranes both on the x and the y axis.

Table 3.4. Simulation time for each value of the field in CG simulations

Field (V/nm)	Simulation time (ns)
0.085	300
0.100	300
0.200	300
0.300	10
0.400	2
0.500	1

In both cases, the field was applied perpendicular to the membrane surface, in order to mimic the physiological conditions, in which the electric field is directed from outer to inner layer (see Figure 3.3). In GROMACS, an external electric field is introduced in the system as an additional force acting on all the atoms charged.

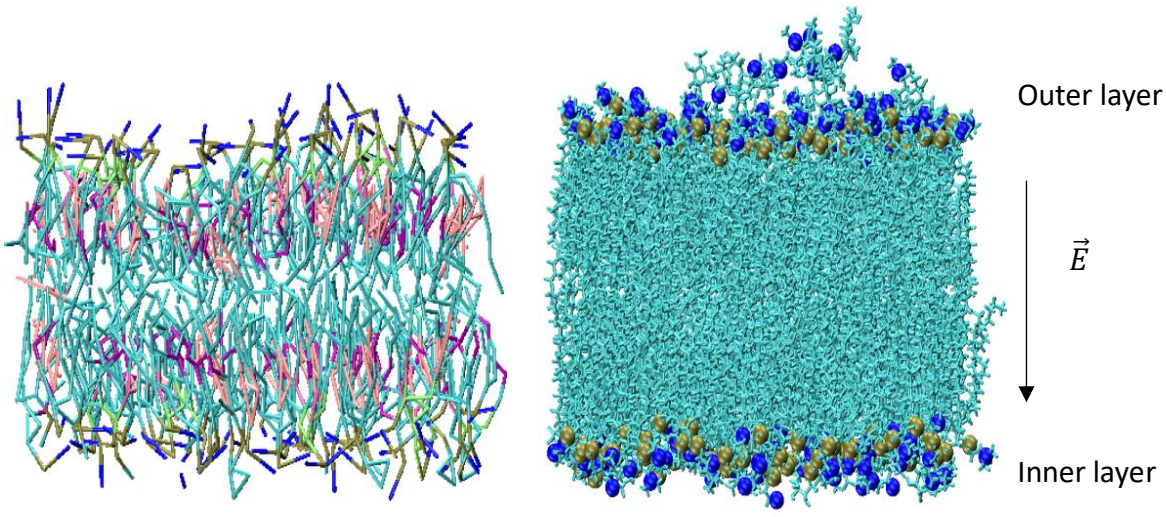

Figure 3.3. Orientation of the field in the voltage-applied simulations.

The pore formation was here defined as the time at which a sudden increase of the total membrane area was observed, as done in previous literature[8]. At this time many water molecules are already in the membrane interior. In fact, the combination of PME electrostatics with the external electric field and the periodic boundaries leads to an artificially enhancing of the local electric fields within the region of the pore. Due to this effect, the pores steadily grow and the membrane collapses in several studies[10]. To overcome this problem, one needs to considerably decrease the external electric field once the pore is formed[10,32]. Mean poration-times were calculated by averaging over the five independent simulation replicas.

The transmembrane potential was approximated as the product between the applied potential and the membrane thickness at the beginning of the simulation. In all-atom simulations, the thickness was calculated as the distance between the two centers of mass of P atoms of the headgroups on each layer. In CG simulations, PO_4 groups were used instead of P atoms.

3.3 Results

3.3.1 AA simulations

It emerged that for values of the potential lower than 0.3 V/nm the pore did not appear in the simulation time in any of the different replicas. Instead, pores appeared in all the replicas with field greater or equal than 0.3 V/nm (see Table 3.5). In the case of a strong field, as in the case of 1 V/Nm, the poration time is almost zero (~200 ps) and the pores appeared immediately. The data suggest an exponential drop of the poration time with the strength of the applied field (Figure 3.4). Moreover, starting from a preformed pore taken from one of the 0.3 V/nm replicas, it was observed that the pore remained stable for values greater or equal than 0.085 V/nm. When a 0.2 V/nm was applied, the membrane was ruptured.

Table 3.5. Pore formation time in the different replicas of the AA models.

Field(V/nm)	**Transmembrane Potential (V)**	**Poration time**	
	(thickness= 4.68 nm)	Time (ns)	Mean (ns)
0.2	0.94	-	-
0.3	1.40	51.35 41.50 68.40 58.45 62.50	56.44±10.40
0.35	1.64	22.25 29.00 28.62 15.60 5.90	20.27±9.72
0.4	1.87	5.77 6.60 7.90 11.40 11.40	8.61±2.65
0.5	2.34	1.80 2.40 2.47 1.85 2.60	2.22±0.37
1.0	0.00	~ 0.2	~ 0.2

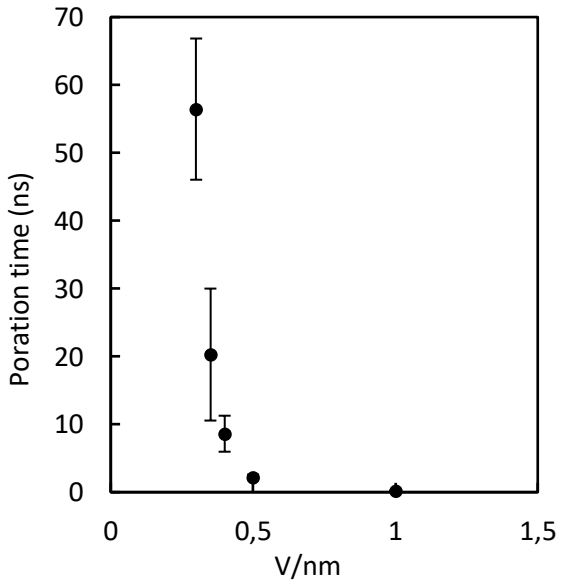

Figure 3.4. Mean poration time at different voltage applied in the AA systems. The error bar is standard deviation. Mean and standard deviation are calculated on the 5 replicas for each value of the field applied. For values lower than 0.3 V/nm no pore was observed in the simulation time.

Figure 3.5 shows the process of pore formation from the perspective of water dynamics. This is the characteristic behaviour observed in all simulations. Pore initiation starts with the application of an external electric field, which perturbs the water-lipid interface, inducing a reorientation of water dipoles. It was pointed out in previous studies[10,33,34] that the asymmetric field gradients at the interface significantly lower the energy barrier for poration. First, protrusions consisting of a few water molecules, often single-file columns, appear on the anodic side of the bilayer (inner layer). Protrusions extend into the bilayer interior and then expands at the base, forming conical structure which eventually bridges the membrane. The radius of the water pore spanning the bilayer then begins to increase. The process is finalized by a considerable reorientation of lipid headgroups towards the membrane interior. The pore expands until the bilayer is ruptured, as explained above.

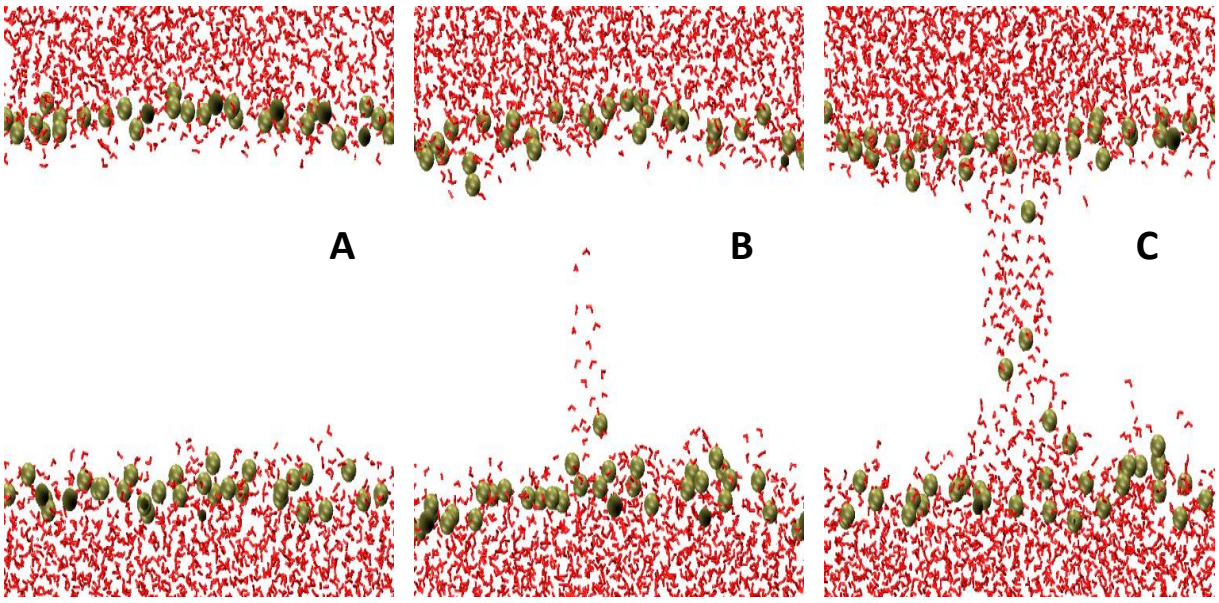

Figure 3.5. Different steps of pore formation time in the case of 0.5 V/nm field applied. Water molecules in red, P atoms of the headgroups in tan.

3.3.2 CG simulations

It emerged that for values of the field lower than 0.3 V/nm the pore did not form in the simulation time in any of the replicas, neither in the bigger system at 0.2 V/nm. Instead, pores appeared in all other field values inspected (see Table 3.6). It is important to underline that in the case of 0.4 V/nm and 0.5 V/nm, pores almost immediately appeared and the membrane

area curve never reached a stable state, but it showed a growing trend since the beginning of the simulation. Again, the data suggest an exponential drop of the poration time with the strength of the field applied (see Figure 3.6). As well as that, it was observed that starting from a preformed pore (pore formation time step of one of the 0.3 V/nm replicas) the pore was stable in a 10 ns time-window for values of the field lower than 0.3 V/nm. In particular, the pore kept being opened for values of the field greater or equal to 0.09 V/nm. It is important to underline that for 0.2 V/nm and 0.1 V/nm the pore growth and led to membrane rupture, while for 0.9 V/nm the pore was stable in the simulation time window. Applying a field of 0.085 V/nm the pore resealed.

Table 3.6. Pore formation time in the different replicas in the MARTINI CG systems

Field (V/nm)	**Transmembrane potential (V)**	**Poration time (ns)**	
	(thickness=4.18 nm)	t (ns)	Mean (ns)
0.085	0.36	-	-
0.1	0.42	-	-
0.2	0.84	-	-
0.3	1.25	6.40 1.60 1.55 5.52 4.00	3.81 ±2.22
0.4	1.67	-	≤ 1
0.5	2.09	-	≤ 0.3

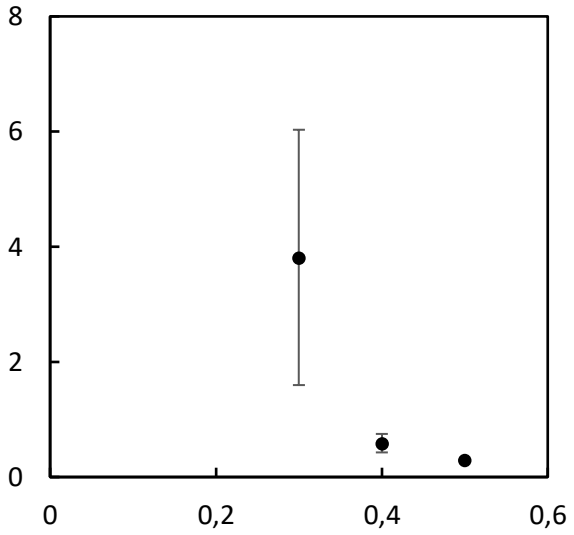

Figure 3.6. Mean poration time at different voltage applied in the MARTINI CG systems. The error bar is standard deviation. Mean and standard deviation are calculated on the 5 replicas for each value of the field applied. For values lower than 0.3 V/nm no pore was observed in the simulation time.

In Figure 3.7 the process of pore formation is showed from the perspective of water dynamics. The process followed the same steps as in the AA simulations. The perturbation at the water-lipid interface and the consequent lowing in the energy barrier for poration, led to the appearance of water protrusions inside the bilayer, this time more frequently on either side of the membrane. Then, protrusions expanded and bridged the membrane. The radius of the water pore spanning the bilayer then began to increase. Finally, lipid headgroups reoriented towards membrane interior and lined the pore. The enhancing of the field in the pore region due to PBC and PME method, led to membrane rupture.

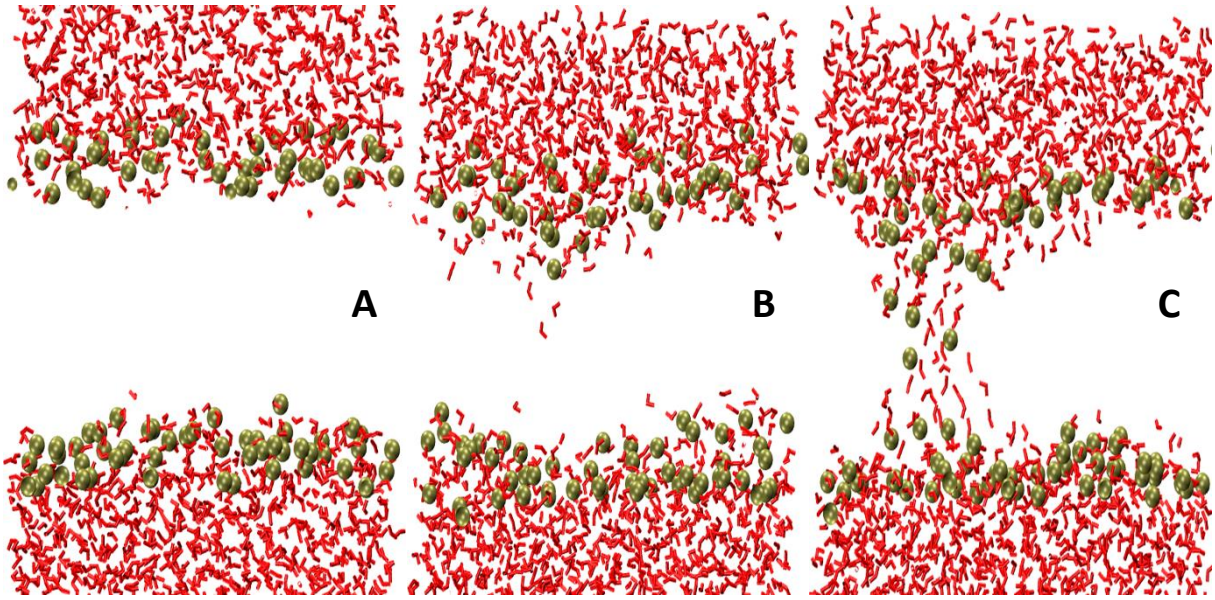

Figure 3.7. Different steps of pore formation time in the case of 0.3 V/nm field applied. Water molecules in red, PO_4 of the headgroups in tan.

3.4 Discussion

In previous studies[35], it was pointed out that the motion of dipoles at the interface, where strong field gradients appear, is the driving force of pore formation when an electric field is applied. In particular, the altered orientation of water dipoles, emerges to be the dominant effect and lead to a cascade of events which ends with a pore. In fact, water pores appeared even in lipid-free systems[36]. It is worth to highlight that the field gradient is always present at the interface, even in the absence of the electric field, but this appears to be balanced by other forces. When an electric field is applied, the balance is broken and pore formation is the way to minimize the total free energy of the system[37]. An external electric field thus leads to a decrease, proportional to the intensity of the field applied, in the energy barrier of water molecules passing across a membrane[38]. Simulations showed, both in the case of AA models and in the case of CG models, how a pore forms in detail. The external electric field forces water molecules to enter into the membrane. Water molecules are followed by the movement of lipid headgroups, which rotate towards the membrane interior thus forming the hydrophilic pore surface. Results suggest that there is a critical intensity of the electric field, which allows inducing pore formation in the membrane-model. This threshold seems to be 0.3 V/nm in the simulated membrane system. Given the stochastic nature of electroporation, it is worth highlighting that the interpretation of the computed threshold has to be taken with care. It

was proposed that the minimal potential threshold to produce a pore within a certain time depends on lipid properties such as the chain length and the type of acyl chains. In particular, a greater number of carbons and unsaturated bonds in the fatty acid chains provoked an increasing in the field required to see pore formation[9]. In addition, early papers[39,40] pointed out that also the presence of cholesterol changes the minimal electric field necessary to porate the membrane on a given timescale. In fact, a large amount of cholesterol enlarges the threshold for electroporation by elevating the lipid ordering. In all simulations in which a pore appeared, the pore grew uncontrolled leading to membrane rupture; that is one of the main drawbacks of the method. This pore-formation process is in line with the typical pore formation process seen in earlier studies presented in literature[11,33,34,36,41] and it is consistent with experimental observations[42]. Concerning the location of pore initiation, it was observed that always happened at the anodic side (inner leaflet) in AA simulations, while it involved either side in CG simulations. It was proposed elsewhere that the pore initiation side depends on lipid properties[9], however divergences exist in literature. When the field was decreased after the pore formation reached at a higher value of the field, it was observed that it is possible to obtain a stable pore by applying a lower transmembrane potential, as seen previously[32]. This suggests that the pore size may be modulated by the electric field after pore formation and that once the pore opened, the energy to keep it open is lower. In all simulations performed, pore formation times are comparable to ones obtained in previous works[11,34], albeit the complex physiological-like membrane composition considered in the current study was never used before.

In both simulation approaches, it emerged an exponential drop of the poration time with the strength of the applied field, which is in agreement with previous studies[11,38]. The main difference in AA and CG simulations is in the poration-time. Considering the same value of the field, in the CG simulations poration-times are lower than in AA simulations, as one could expect. In fact, it is well known that the Martini CG approach took a speed-up in the time-scale of the simulations.

The field values investigated are far from being physiological values (hundreds of mV) of the transmembrane potential. However, they are comparable to values of the transmembrane voltage used for electroporation in experiments[18] and previous simulations[38,39,41]. Further simulations we performed seems to suggest a strong correlation between the amount of

water and the number of lipids. When the lipid/water ratio decreases, the poration field threshold lower consequently. However, such exaggerated potential allowed viewing pore formation in reasonable time scales and reducing the computational effort.

3.5 Conclusions

A comprehensive microscopic description of electroporation process is a complicated task to be performed experimentally, due to nanoscale dimensions of the pore and to the short time scale (ns) of pore formation. For these reasons, simulations became hugely important, since they can overcome the experimental limits. The simulations performed in this work proceed in this direction and showed that nanoscale pores can be formed under the application of an external constant electric field in complex physiological-like cell membranes. A variety of different values of the field was investigated both in all-atom and coarse-grained simulations. It emerged that in both cases the poration happened in comparable time-scales (tens of nanoseconds), with a speed-up of the process, as expected, in CG simulations. To overcome the membrane rupture due to the enhancement in pore dimensions and to obtain a stable pore, the two-steps protocol proposed elsewhere[32], which consists in the decreasing of the field after the pore formed, revealed to work fine. The pore-formation time resulted to be modulated by the intensity of the field applied, even though it was demonstrated in literature that the voltage threshold for electroporation is influenced by many factors like bilayer composition, cholesterol percentage, patch-size.

4 CPP direct penetration through water pores driven by ionic imbalance in coarse-grained simulations

Cell penetrating peptides have demonstrated the ability to penetrate the plasma membrane and this potential have led to the development of drug-delivery strategies, which combine the action of these peptides with active cargoes. However, the uptake pathway has not yet fully clarified. Both endocytosis and direct translocation through membrane pores have been observed experimentally and in simulations. In the present work, molecular dynamics simulations provided evidence of the influence of transmembrane potential in driving the direct translocation of cell penetrating peptides. In particular, the focus was on mimicking hyperpolarized conditions, which were reported to be typical in cancer cells, by imposing ion imbalance across the membrane. The charge and the peptidic sequence resulted to be key feature to see direct translocation.

4.1 Introduction

Cell penetrating peptides (CPPs) are a family of various non-toxic peptides, typically comprising 5-30 amino acids, which can pass through tissues and cell membranes via energy-dependent or –independent mechanisms without interactions with specific receptors. These peptides showed the capacity of transporting a variety of biological cargoes into cells, including proteins, small drugs, DNAs and nanoparticles. These cargoes can be bound to CPPs covalently or non-covalently[43]. More than 100 peptidic sequences were described that are capable of internalization into mammalian, plant and bacterial cells[44]. Despite CPPs are more frequently used in research, they did not reach a clinical use because their uptake pathways have not been fully understood, yet. However, some preclinical evaluations and clinical trials with CPP-derived therapeutics provide promising results. There are many classification-criteria proposed for CPPs. Based on their origin, they can be classified in protein-derived peptides, model peptides and designed peptides. According to their physical-chemical properties, they can be distinguished in three main classes: cationic, amphipathic and hydrophobic peptides. Cationic peptides present positive charge at physiological pH, principally due to arginines and lysines. TAT-derived peptides, penetratin and polyarginines belong to this class. Amphipathic CPPs contain both polar and non-polar regions (valine, leucine, isoleucine and alanine). Some amphipathic CPPs usually assume an α-helical

conformation, like model amphipathic peptide (MAP) and Transportan. Alternatively, they can acquire a β-sheet structure on interaction with a phospholipid membrane. Hydrophobic class contain nonpolar residues, with high affinity for the hydrophobic domains of cellular membranes. An example of hydrophobic CPPs is the Pep-7.

The uptake of CPPs is strongly influenced by their properties, their concentration, attached cargo and, in some cases, cell type. Therefore, the entry route for CPPs is a controversial issue and the pathways involved are not fully clear. Two types of uptake mechanisms coexist and operate concomitantly: direct penetration through the lipid bilayer and endocytosis (see Figure 4.1). The process of direct penetration is initially based on the electrostatic interaction between the positively charged CPPs with the negatively charged membrane's inner layer components. The interaction is followed by the translocation of the peptide across the bilayer via various mechanisms causing the formation of a transient pore[45,46] or membrane destabilization. Endocytosis is the principal internalization route for many CPPs and can involve a number of pathways classified as micropinocytosis, clathrin- or caveolin- mediated endocytosis and clathrin/caveolin independent endocytosis. CPPs have been successfully used to mediate the delivery of several molecules in different cell types and have the potential to increase the transfer of many other active agents. The main drawbacks of using CPPs are linked to their not fully understood uptake mechanisms and their general lack of cell and tissue specificity, which can be overcome by functionalization or binding to targeted cargoes. Here, the focus is on the direct penetration through hydrophilic pores driven by a transmembrane potential. In fact, the effect of the membrane potential was rarely taken into account when investigating CPP translocation. To demonstrate the essential role of the transmembrane potential in CPP penetration, a double bilayer system with ionic imbalance was constructed. The interest was mainly to model hyperpolarized conditions, which are typical in cancer cells, to direct and to improve the development of drug-delivery strategies. The translocation of seven different peptides was investigated:

- Model Amphipathic Peptide, known as MAP (KLALKLALKALKAALKLA) is a alanine/leucine/lysine-rich chemically synthesized peptide.
- Penetratin or $pAntp_{43-58}$ (RQIKIWFQNRRMKWKK) is a cationic 16-amino-acid peptide corresponding to the third helix of the Drosophila Antennapedia homeodomain.
- Pep-7 (SDLWEMMMVSLACQY) is a hydrophobic CHL8 peptide phage clone.

- ARG_9 (RRRRRRRRR) is a cationic polyarginine peptide which is chemically synthesized.
- TAT_{48-57} (GRKKRRQRRR) is a ten amino-acid fragment derived from the trans-activator of transcription HIV-1 protein.
- TAT_{48-57} -$RasGAP_{317-326}$ (GRKKRRQRRRGGWMWVTNLRTD) is made up of the CPP TAT_{48-57} and a 10 amino amino-acid sequence derived from the SH3 domain of p120RasGAP, which is a protein involved in various functions such as anti/pro apoptosis, proliferation and also cell migration[47]. TAT-$RasGAP_{317-326}$ sensitizes cancer cells to chemo-, radio- and photodynamic therapies and prevents cell migration and invasion[48–52]. Moreover, it was discovered that this RasGAP-derived peptide possesses the ability to directly kill some cancer cells[53].
- Transportan (GWTLNSAGYLLGKINLKALAALAKKIL) is a 27 amino acid chimeric galanin-mastoparan amphipathic peptide.

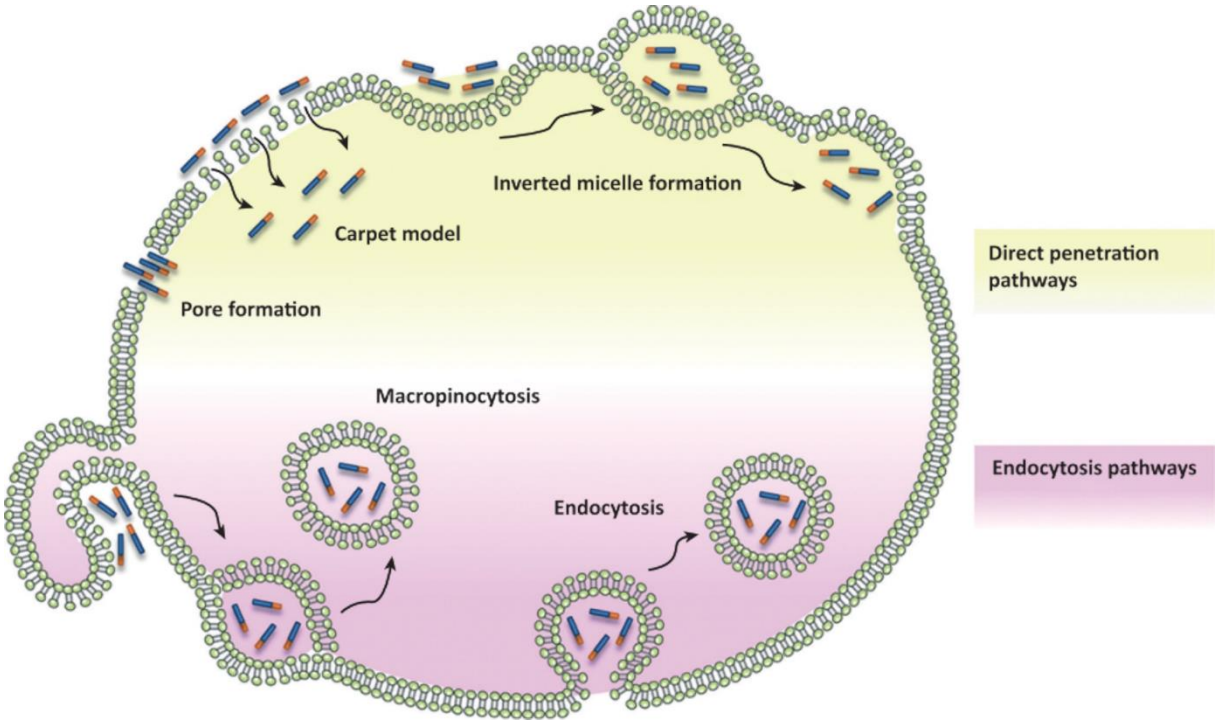

Figure 4.1. Representation of proposed mechanisms for CPPs uptake. The internalization pathways can be divided in 2 groups: direct translocation (green) and endocytosis (purple).

4.2 Materials and methods

4.2.1 System coordinates and topologies

The molecular system of an asymmetric multi-component bilayer was constructed and solvated using CHARMM-GUI[19,20]. Each layer contained 100 lipids and it was composed as indicated in Table 4.1. From this bilayer, a double bilayer system was constructed and the system in Figure 4.2 was obtained. The system consisted of about 17000 particles. The martini22p (Martini 2.2 polar amino acids, Martini 2.0 lipids and polarizable water) MARTINI[6,30] force field was used to define lipid and explicit water topologies through a coarse-grained approach.

Table 4.1. Composition of each bilayer.

	Inner Layer		**Outer Layer**	
Type	**#**	**%**	**#**	**%**
POPC	18	18	39	39
POPE	27	27	6	6
PSM	10	10	21	21
POPS	11	11	-	-
POPI	5	5	-	-
CHOL	29	29	34	34
Total	100	100	100	100

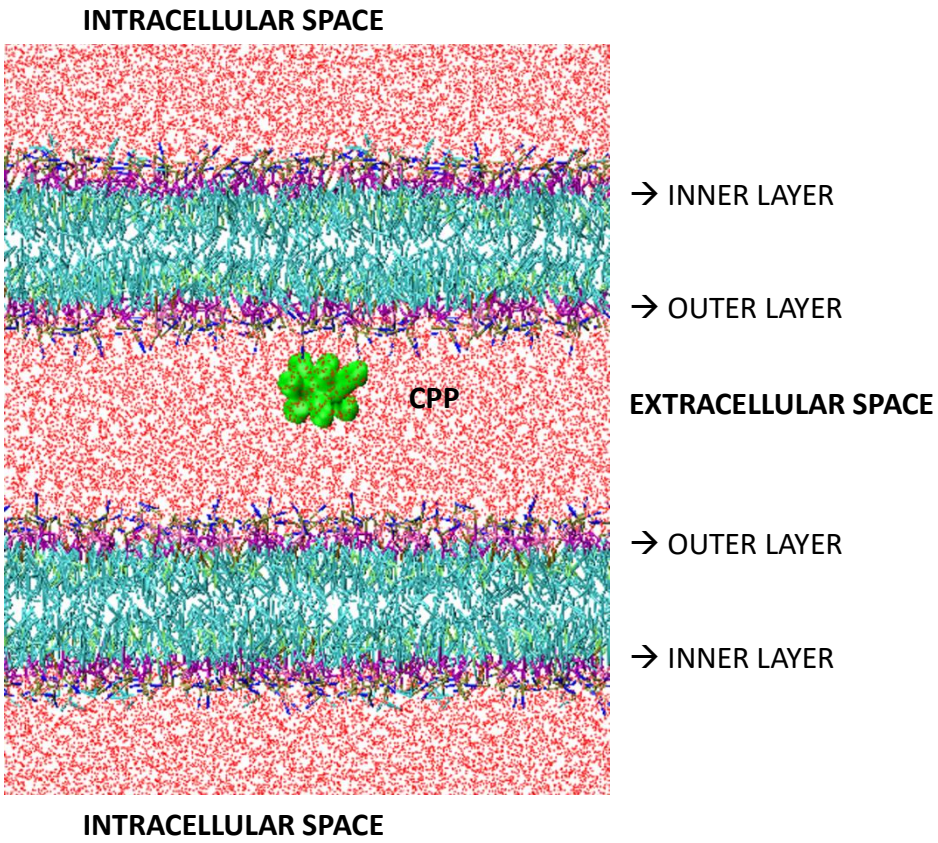

Figure 4.2. Visual inspection of the double bilayer system.

4.2.2 Cell penetrating peptides (CPP)

Seven different CPPs were considered, as reported Table 4.4. For each molecular system, the CPP was positioned in the middle of the extracellular space, 3 nm far from each membrane outer leaflet. Considering the ion's concentration of a hyperpolarized membrane (see Table 4.2, Table 4.3), the net charge difference between intracellular and extracellular space is about 15 positive ions for each bilayer. Thus, a total ion imbalance of 30 positive charges was generated in all simulated systems, keeping into account all the charges of the system (see Table 4.5). Hyperpolarizing conditions are interesting because it was observed that many cancer cell types possess a more depolarized transmembrane potential than cells in normal tissues[54].

Table 4.2. Ionic concentration of a membrane in resting conditions.

Ions	Extracellular	Intracellular
Na^+	150 mM	15 mM
K^+	5 mM	120 mM
Cl^-	120 mM	20 mM
Ca^{++}	1 mM	100 nM

Table 4.3. Ionic concentration of a hyperpolarized membrane[55,56].

Ions	Extracellular	Intracellular
Na^+	150 mM	15 mM
K^+	20 mM	105 mM
Cl^-	120 mM	20 mM
Ca^{++}	1 mM	100 nM

It is important to underline that the condition of electroneutrality in the whole system was fulfilled. To analyse whether the CPPs were able to penetrate the membrane and reach the intracellular compartment, last 5 ns of trajectories were studied defining 3 sectors the CPP could be in: intracellular, extracellular, membrane. These 3 compartments were defined on the basis of the z-coordinates (Z) of the CPP's COM and the Solvent Accessible Surface Area (SASA) of the CPP, which allows discriminating the cases the CPP is at the water-lipid interface. The z-coordinates of the COM of outer layer PO_4 groups (Z_o) and inner layer PO_4 groups (Z_i) were computed. If Z was between the Z_o coordinates and the value of the SASA was bigger or equal to 40% of the SASA at the beginning of the simulation, the CPP was considered to be in the extracellular space. If the Z value was between Z_o and Z_i and the SASA was lower than the previous cut-off value, the CPP was considered inside the membrane. If $|Z|$ was greater than $|Z_i|$ and the CPP was solvated (SASA greater than the cut-off value), it was considered penetrated in the intracellular space.

Table 4.4. Cell Penetrating Peptides considered in the present study.

Name	Sequence	Class
MAP[57]	KLALKLALKALKAALKLA	amphipathic
Penetratin$_{43-58}$ [58] (pantp)	RQIKIWFQNRRMKWKK	cationic
Pep-7[59] (pep)	SDLWEMMMVSLACQY	hydrophobic
R9[60]	RRRRRRRRR	cationic
TAT$_{48-57}$[61] (tat)	GRKKRRQRRR	cationic
TAT-RasGAP$_{317-326}$ (tatrasp)	GRKKRRQRRRGGWMWVTNLRTD	amphipathic
Trasportan[62] (tran)	GWTLNSAGYLLGKINLKALAALAKKIL	amphipathic

Table 4.5. Distribution of the charges in the systems simulated. All charges present in the sysem were considered (CPP, ions, lipids).

	CPP charge	intracellular ions		extracellular ions		membrane		
		NA	CL	NA	CL	inner layer	outer layer	total imbalance
Map	5	17	0	17	-7	-32	0	30
Pantp	7	17	0	17	-9	-32	0	30
Pep	-2	17	0	17	0	-32	0	30
R9	9	17	0	17	-11	-32	0	30
Tat	8	17	0	17	-10	-32	0	30
Tatrasp	8	17	0	17	-10	-32	0	30
Tran	4	17	0	17	-6	-32	0	30

4.2.3 Water pore formation

Considering that more than one pore appeared in some of the simulations, porated membrane was divided into 4 sectors on the x-y plane. Poration time was calculated as the time at which at least 8 water molecules were in the central region of the membrane in one of this four sectors. The central region was considered as a 1nm slab along z-axis around the

membrane's COM. This method is different from the method used in chapter 3, which cannot be employed because in the ion imbalance approach the membrane does not collapse, hence the sudden increase in bilayers area does not occur. However, the results obtained in poration time are coherent between the two methods.

Since the transient water pores induced by ionic charge imbalance are subject to considerable fluctuations in size, and their shape is non-uniform across the membrane, only a rough estimate of the pore size was possible. The radius of the pore in the membrane interior was calculated as in previous works[63,64]. It was assumed that the central part of a pore contains N_{water} molecules at the same density as in bulk water and that it is cylindrical in shape. Since the MARTINI CG approach was employed, the number of water molecules was multiplied to 4, to obtain values comparable to all atoms simulations. In some membrane s, more than 1 pore formed in the simulation time; in these cases the greater one was considered.

The ionic imbalance at the end of simulations was computed, as well. First the center of mass for both bilayers was calculated. Based on these values, ions were assigned to intracellular or extracellular space, according to their z coordinates.

4.2.4 Simulation setup

Simulations were performed using the GROMACS 5.1.4[22] and GROMACS 2016.3[22] software packages. First, each system was subject to energy minimization through steepest descent[23] algorithm and then it was undergone to a process of equilibration passing through three NPT runs with a 2 fs, 10 fs, 20 fs time step respectively. Velocity rescaling[31] temperature coupling algorithm and time constant of 1.0 ps were applied to keep the temperature at 303.15 K. Berendsen[24] semiisotropic pressure coupling algorithm with reference pressure equal to 1 bar and time constant 5.0 ps. All systems were simulated in the NPT ensemble. A 20 fs time step was used. Electrostatic interactions were calculated with the particle-mesh Ewald (PME)[25] method and van der Waals interactions were defined within a cut-off of 1.2 nm. Velocity rescaling[31] and Parrinello-Rahman[27] coupling methods were used as temperature and semiisotropic pressure coupling, respectively. Time constant was equal to 1 ps for temperature, while it was equal to 12 ps for pressure. The bilayers and the solvent were coupled separately in temperature. In addition, the center-of-mass motion removal was done separately for these groups. Periodic boundary conditions were applied in all directions. The

final step of the equilibration runs was taken as starting configuration for electroporation MD simulations. Trajectories were collected every 10 ps and the Visual Molecular Dynamics (VMD)[29] package was employed to display the simulated systems.

4.3 Results

4.3.1 Water pore formation

Ten different 100 ns replicas of MD simulations were performed in order to study the ability of each CPP to cross the membrane through a water pore induced by ionic imbalance. It is worth mentioning that in all MD simulations, it was observed a water pore formation in tens of nanoseconds, according to the data presented in Figure 4.3 and Table 4.6, which underline the stochastic nature of pore formation. In all simulations, only one membrane was porated. The only exception was one of the replicas of the PEP, in which a pore appeared in both membranes. Moreover, five 100 ns simulation replicas were run under the same ion imbalance conditions without the presence of CPPs and pointed out that poration happened as well.

Table 4.6. Pore formation time for each simulation performed. The first column indicates if the pore appears in the upper membrane (U) or in the lower one (D). In the last row, average times and standard deviations are indicated.

map		**pantp**		**pep**		**r9**		**tat**		**tatrasp**		**tran**	
	t (ns)		t (ns)		t (ns)		t (ns)		t (ns)		t (ns)		t (ns)
U	3.04	D	2.08	D	0.64	D	2.32	D	4.02	D	17.96	D	4.10
D	14.00	U	8.28	D	6.54	U	3.80	U	1.60	D	4.16	D	1.78
D	0.88	U	1.30	U	5.10	D	32.54	U	2.32	U	2.60	D	8.86
D	3.40	D	1.10	U	0.48	U	6.86	U	2.62	U	1.08	D	3.68
D	12.10	D	1.00	D	1.48	U	0.82	D	20.58	U	5.36	U	3.60
U	6.86	U	0.74	U	2.48	U	1.42	U	0.80	U	2.26	D	0.94
U	1.56	D	2.34	U	2.52	U	4.74	D	4.30	U	2.30	U	0.90
D	12.44	D	2.00	U	3.42	U	3.40	D	1.24	D	1.56	U	1.40
U	3.48	U	0.92	D	5.64	U	1.18	D	77.92	D	3.30	U	1.80
U	5.84	D	2.02	D	3.62	D	3.10	U	2.42	U	0.92	D	2.66
6.36 ±4.83		2.18 ±2.22		3.19 ±2.08		6.02 ±9.49		11.78 ±23.95		4.15 ±5.04		2.97 ±2.37	

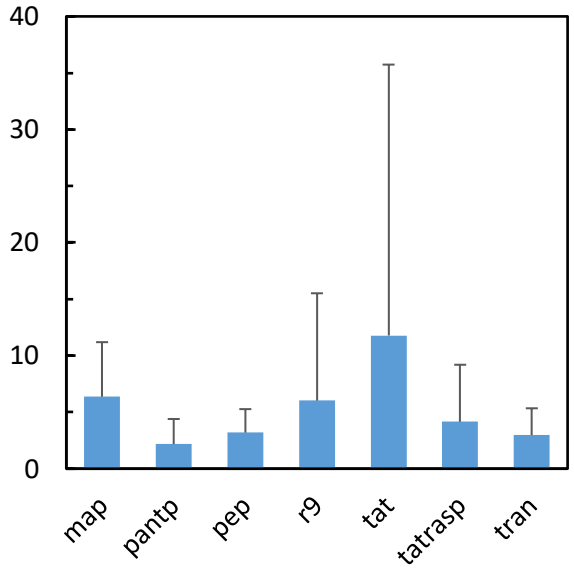

Figure 4.3. Mean pore formation time for each peptide. Bars represent standard deviation.

In detail, the hyperpolarization of the membrane implied a perturbation of the water-lipid interface, inducing a reorientation of water dipoles. It was pointed out in previous studies that the asymmetric field gradients at the interface significantly lower the energy barrier for poration[10,33,34]. The picture of pore formation (Figure 4.4) is the same to what is observed in electroporation studies under the influence of an external applied field (seen in Chapter 3). First, a single water wire appeared either side of the bilayer, spanning the bilayer. A protrusion extended into the bilayer interior and then expanded at the base, forming a conical structure, which eventually bridged the membrane. The radius of the water pore then began to increase. The process is finalized by a considerable reorientation of lipid headgroups towards the membrane interior. Polar lipid headgroups migrated from the membrane-water interface to the interior of the bilayer, forming within hydrophilic pores that surrounded and stabilized the water columns[11,33,34,36,41]. In addition, a transport of ions was observed and it led to a considerable drop in the transmembrane voltage, so to a reduction in pore dimensions. In fact, pore resealed and lipids headgroups came back towards the membrane. The resealing process is in opposition to what is observed in a membrane porated by an external field, which can only be resealed if the field is removed or reduced under a certain threshold.

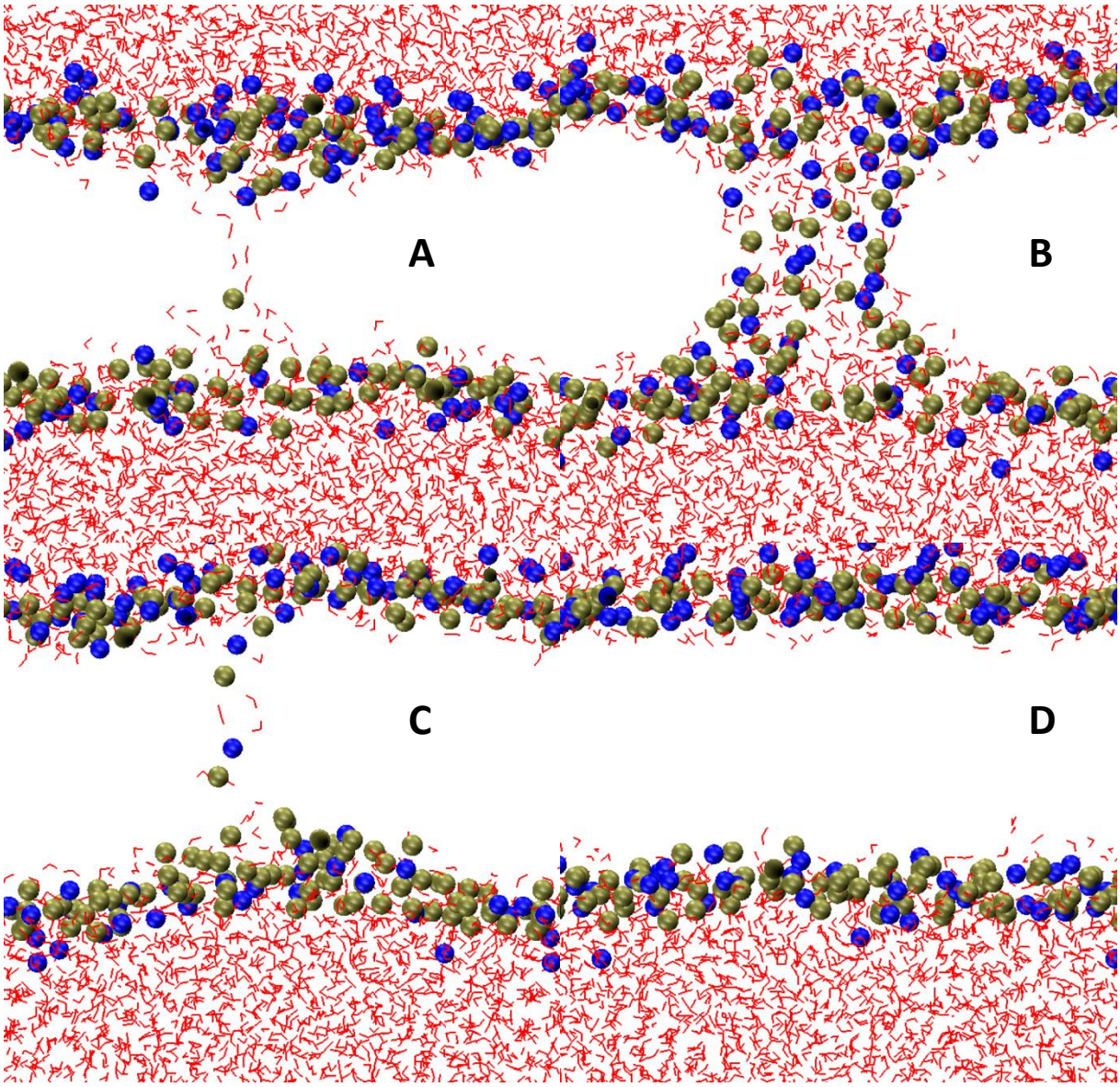

Figure 4.4. Steps of pore formation and resealing. A) Beginning of poration, a water wire appears spanning the membrane. B) Completely developed pore, with a hydrophilic wall of the lipid-headgroups. C) Resealing process. D) Completely resealed membrane. PO_4 groups in tan, NC_3 groups in blue.

For what concerns the ion flow, a major permeation of Na^+ ions from extracellular to intracellular space was witnessed, while the permeation of Cl^- (when present in the system) was found to be a rare event. It emerged that the ion flow never led to the re-equilibration of the charge-imbalance in the system, due to the fact that under a certain potential threshold pores closed (see Figure 4.5).

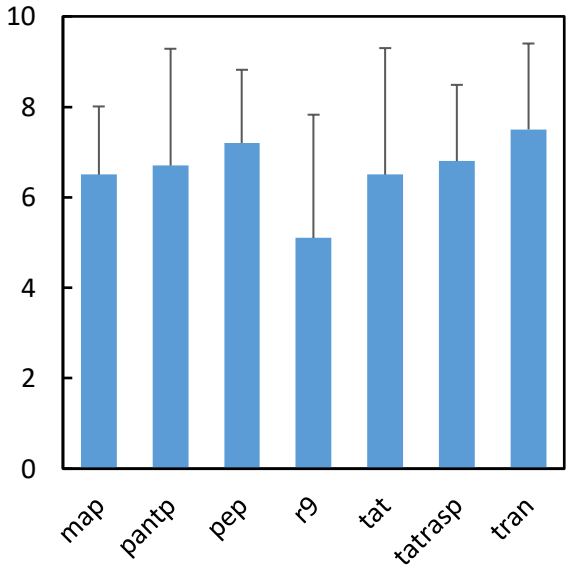

Figure 4.5. Na^+ ions mean flow from extracellular to intracellular space in the different systems. Cl^- ions mean flow is not present because it is rare and when it emerged, it was ≤0.1.

4.3.2 CPPs penetration mechanism

Ten different 100 ns replicas of MD simulations were performed in order to study the ability of each CPP to move from the extracellular to the intracellular space.

The Cell Penetrating Peptides' translocation ability was evaluated by considering the number of time-steps the CPP spent in the intracellular space, averaged over the ten MD replicas. The results, reported in Figure 4.6 and Table 4.7, show how the membrane hyperpolarization was able to drive the CPP translocation mechanism. In particular, R9 and TAT peptide were able to cross the membrane and reach the intracellular space. The CPP spent in the intracellular space the 41.1 % and 18.4% of time, considering the last 5 ns of the simulated replicas, respectively. In addition, TATRASP and PANTP were able to cross the extracellular barrier in some cases (see Figure 4.7). The dynamic process can be described as follows. Firstly, the CPP in water got in touch with the membrane. Then, a pore formed, disturbed the lipid arrangement leading to a local thickness decrease and the CPP moved towards the intracellular space. PEP was unable to reach the intracellular compartment, probably because of its negative charge, even though in some cases it demonstrated ability to move inside the membrane. It is worth highlighting the peculiar behaviour of MAP. Despite its ability to penetrate the intracellular membrane in some of the simulated replicas, it remained trapped into the intracellular

membrane, probably because of its amphipathic nature. In best cases, visual inspection demonstrated that it remained trapped among the lipids headgroups on the intracellular space. The same behaviour seems to be proper of the TRAN, even though in few cases it reached the intracellular space. In this sense, it is important the information given by Figure 4.8, which describes in detail where the CPPs located during simulations and remarks that even in case of penetration, the CPPs remained in membrane proximity, maybe due to electrostatic interactions. For this reason, it was important to consider the SASA in determining CPPs' location to discriminate cases at the water-lipid interface.

Further simulations were performed without the application of the membrane-hyperpolarized potential, showing that, in all cases, the CPPs remained in the extracellular space and no pores formed. In addition, simulation with the same ionic imbalance and without the presence of CPPs pointed out that poration happened likewise.

Table 4.7. Frequency (in %) of finding the peptide in a different sector (intracellular, extracellular, membrane) averaged over the last 5 ns of simulation for all the replicas.

CPP	intracellular	membrane	extracellular
map	0.0	99.8	0.2
pantp	4.8	49.6	45.6
pep	0.0	98.3	1.7
r9	41.1	21.9	37.0
tat	18.4	28.9	52.7
tatrasp	12.5	33.7	53.8
tran	0.4	69.4	30.2

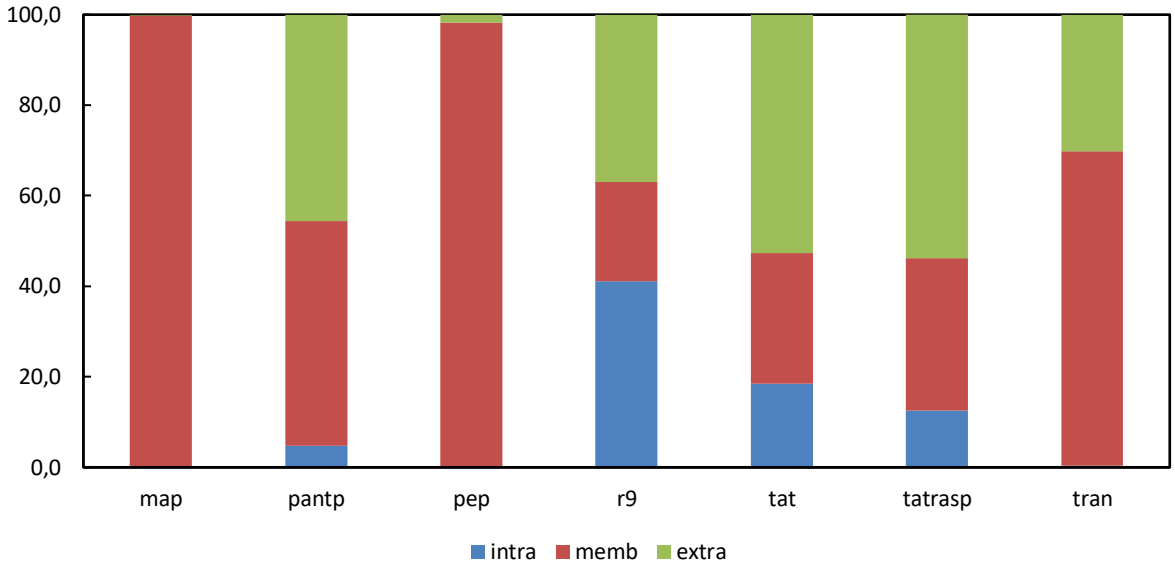

Figure 4.6. Frequency (in %) of finding the peptide in a different sector (intracellular, extracellular, membrane) averaged over the last 5 ns of simulation for all the replicas.

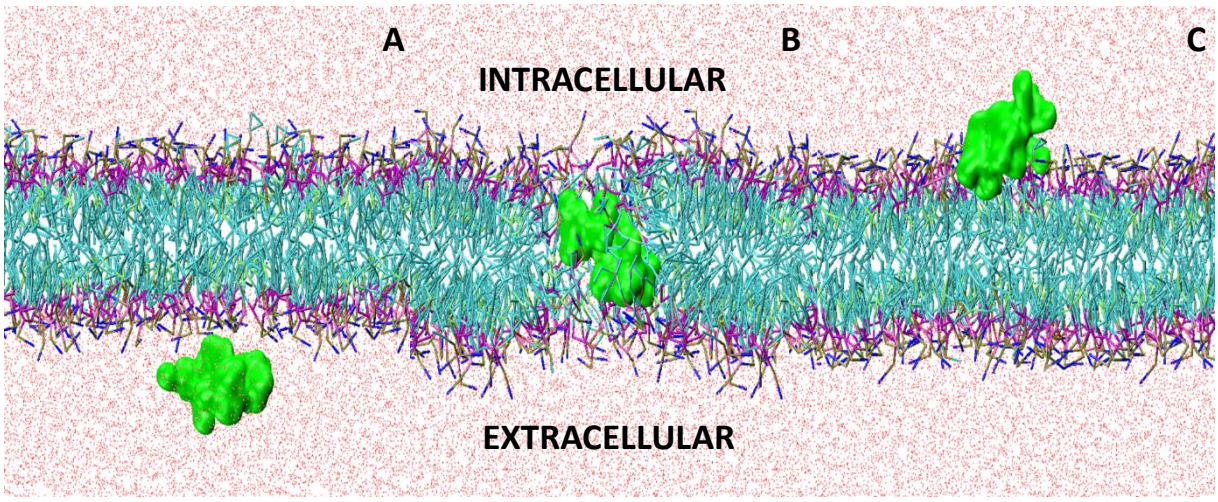

Figure 4.7. Visual inspection of the penetration process of TAT-RASP. A) Extracellular space. B) Membrane penetration. C) Reaching the intracellular space.

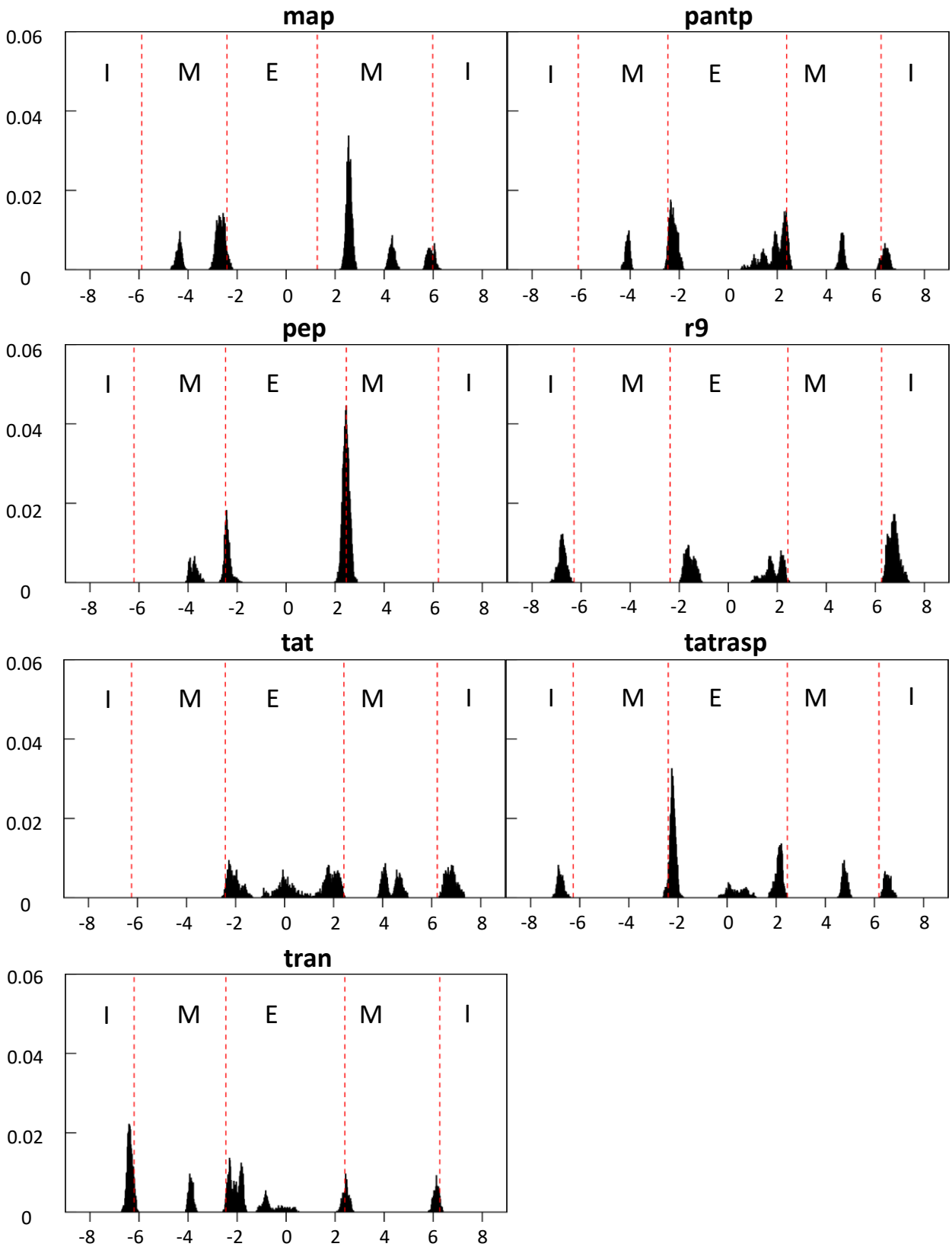

Figure 4.8. Frequency distribution (in %) of the distances (in nm) from protein's COM to system's COM along the z coordinate. The dotted lines in red represent the mean distances from the PO4 membrane-layer-headgroups' COM to system's COM. The distribution is obtained averaging over the replicas, taking the last 5 ns of simulation from each replica. The capital letters indicate the compartments: E is the extracellular space, I the intracellular space, M the membrane space.

4.4 Discussion

Previous works[64] already noticed that only one membrane porated when a potential is applied through the application of ion imbalance, as it was observed in the present study. This seems due to the fact that the poration in one of the membranes significantly reduces the probability of seeing poration in the other one. As explained, the pore formation process is the same that was observed when an external electric field was applied (seen in Chapter 3) and it is in line with studies already appeared in litterature[35,65]. In all simulations, poration happened and did not result to be linked to the presence of CPPs. In fact, simulation performed in absence of the CPPs indicated the pore formed in any cases under the same ion imbalance. In a similar recent study performed on a DPPC membrane it was pointed out that in absence of CPPs a ion imbalance of 5 is the threshold to see pore appearance. They also noticed that in presence of the CPPs, a lower ionic imbalance was required for water pore formation[66]. Further simulations performed suggest a strong correlation between the amount of water molecules and the number lipids. An increase in water leads to a consequent decrease in poration field threshold, permitting to observe a pore with a lower charge imbalance.

The ion flow involved almost solely Na^+ ions and did not lead to a re-balance of the charges, because the pore closed before, in consequence of the drop in the transmembrane potential, which is one of the main shortcomings in the double bilayer setup. This feature is in agreement with antecedent literature[64,67].

It was demonstrated that direct translocation involves multiple entry routes that are initially based on the electrostatic interaction between the negative charged membrane components and the positively charged CPPs[43]. This issue seems to be confirmed by the fact that the PEP, the only negative charged CPP in this study, did not cross the membrane. However, electrostatic interactions cannot explain completely the translocation process; otherwise one should expect to see penetration for all positive-charged peptides. From the results, it emerged the importance of the water pore driven by the transmembrane potential in the CPP translocation across the membrane. As a matter of fact, simulations in which the potential was not applied, showed no translocation in any cases. This is in line with what emerged before in simulations and experimentally[66,68,69]. Analysing singularly the uptake of the different CPPs, came out that R9 presented a high uptake percentage, TAT e TATRASP a medium uptake percentage, PANTP a low uptake percentage and TRAN an almost nihil uptake.

Experimental results[70] indicated high level of uptake for PANTP, TRAN, MAP and R9 and medium uptake for TAT, albeit the influence of membrane potential was not taken in consideration and the main internalization pathway was the endocytosis. However, there is increasing evidence that arginine-rich cell-penetrating peptides including Tat, Penetratin and oligoarginine peptides are internalized also by direct internalization[71]. The major affinity for translocation of R9, TAT and PANTP appeared in experimental studies too[72]. It was proposed that the number of the amino acids in the peptidic sequence, in particular arginine, it is critical in determining the uptake, thanks to its guanidinium group that have the peculiar property of forming bidentate hydrogen bonds with carboxylic, sulphate and phosphate groups of cell membrane. In contrast, ammonium cations in lysines can donate only one hydrogen bond[43,73]. This aspect seems to be confirmed by the results obtained, as the CPPs that did not present arginine are those that did not translocate in the intracellular environment. Other earlier studies and simulations suggested that the translocation of the CPPs might need a cooperative effect to overcome the high-energy barrier to penetrate membrane, thus depending on peptide concentration. But also cell type, membrane-lipid composition, peptide's charge and its structural characteristics play an important role[74,75].

Finally, a remarkable aspect in translocated CPPs in simulations is their proximity to membrane, probably due to electrostatic interactions.

4.5 Conclusions

In summary, coarse-grained molecular dynamics simulations revealed the mechanism of CPPs translocation through cell membranes driven by potential in hyperpolarizing conditions. The results demonstrated that the membrane potential, recreated by ionic imbalance, plays an essential role in translocating CPPs across the membrane. In particular, the creation of a hydrophilic pore, usually in tens of nanoseconds, was witnessed to be the pathway for penetration. The observations suggested the importance of CPP's charge and a strong influence of arginine residues in such pathway, as was observed also experimentally. It was demonstrated by experimental evidences that CPPs could enter the cell mainly via endocytosis. However, direct penetration modulated by hyperpolarizing membrane potential may be exploited and further enhanced in future drug-delivery strategies.

5 References

(1) Leach, A. R. *Molecular Modelling : Principles and Applications*, 2nd ed.; Prentice Hall, 2001.

(2) Hollingsworth, S. A.; Dror, R. O. Molecular Dynamics Simulation for All. *Neuron*. September 2018, pp 1129–1143. https://doi.org/10.1016/j.neuron.2018.08.011.

(3) Abraham, M.; Apol, E.; Apostolov, R.; Berendsen, H. J. C.; Van Buuren, A.; Bjelkmar, P.; Van Drunen, R.; Feenstra, A.; Fritsch, S.; Groenhof, G.; et al. GROMACS USER MANUAL Contributions from Preface & Disclaimer. **1991**.

(4) Ramachandran, K. .; Deepa, G.; Namboori, K. *Computational Chemistry and Molecular Modeling*; Springer Berlin Heidelberg: Berlin, Heidelberg, 2008. https://doi.org/10.1007/978-3-540-77304-7.

(5) Zhou, R. *Molecular Modeling at the Atomic Scale*; 2018. https://doi.org/10.1201/b17282.

(6) Marrink, S. J.; De Vries, A. H.; Mark, A. E. Coarse Grained Model for Semiquantitative Lipid Simulations. **2004**. https://doi.org/10.1021/jp036508g.

(7) Marrink, S. J.; Tieleman, D. P. Perspective on the Martini Model. *Chem. Soc. Rev.* **2013**, *42* (16), 6801–6822. https://doi.org/10.1039/c3cs60093a.

(8) Fernández, M. L.; Marshall, G.; Sagués, F.; Reigada, R. Structural and Kinetic Molecular Dynamics Study of Electroporation in Cholesterol-Containing Bilayers. *J. Phys. Chem. B* **2010**, *114* (20), 6855–6865. https://doi.org/10.1021/jp911605b.

(9) Ziegler, M. J.; Thomas Vernier, P. Interface Water Dynamics and Porating Electric Fields for Phospholipid Bilayers. *J. Phys. Chem. B* **2008**, *112* (43), 13588–13596. https://doi.org/10.1021/jp8027726.

(10) Böckmann, R. A.; de Groot, B. L.; Kakorin, S.; Neumann, E.; Grubmüller, H. Kinetics, Statistics, and Energetics of Lipid Membrane Electroporation Studied by Molecular Dynamics Simulations. *Biophys. J.* **2008**, *95* (4), 1837–1850. https://doi.org/10.1529/BIOPHYSJ.108.129437.

(11) Gurtovenko, A. A.; Lyulina, A. S. Electroporation of Asymmetric Phospholipid

Membranes. *J. Phys. Chem. B* **2014**, *118* (33), 9909–9918. https://doi.org/10.1021/jp5028355.

(12) Lyubartsev, A. P.; Rabinovich, A. L. Force Field Development for Lipid Membrane Simulations. *Biochim. Biophys. Acta - Biomembr.* **2016**, *1858* (10), 2483–2497. https://doi.org/10.1016/j.bbamem.2015.12.033.

(13) Van Meer, G.; Voelker, D. R.; Feigenson, G. W. Membrane Lipids: Where They Are and How They Behave. *Nature Reviews Molecular Cell Biology*. Nature Publishing Group February 1, 2008, pp 112–124. https://doi.org/10.1038/nrm2330.

(14) Cooper, G. M.; Hausman, R. E. The Cell: A Molecular Approach. *Sinauer Assoc. Inc, Washint. DC* **2009**, No. 1, 355–359. https://doi.org/10.1007/s13398-014-0173-7.2.

(15) Ingólfsson, H. I.; Melo, M. N.; van Eerden, F. J.; Arnarez, C.; Lopez, C. A.; Wassenaar, T. A.; Periole, X.; de Vries, A. H.; Tieleman, D. P.; Marrink, S. J. Lipid Organization of the Plasma Membrane. *J. Am. Chem. Soc.* **2014**, *136* (41), 14554–14559. https://doi.org/10.1021/ja507832e.

(16) Marrink, S. J.; Jähnig, F.; Berendsen, H. J. C. Proton Transport across Transient Single-File Water Pores in a Lipid Membrane Studied by Molecular Dynamics Simulations. *Biophys. J.* **1996**, *71* (2), 632–647. https://doi.org/10.1016/S0006-3495(96)79264-0.

(17) Belehradek, M.; Domenge, C.; Luboinski, B.; Orlowski, S.; Belehradek, J.; Mir, L. M. Electrochemotherapy, a New Antitumor Treatment. First Clinical Phase I-II Trial. *Cancer* **1993**, *72* (12), 3694–3700. https://doi.org/10.1002/1097-0142(19931215)72:12<3694::AID-CNCR2820721222>3.0.CO;2-2.

(18) Chen, C.; Smye, S. W.; Robinson, M. P.; Evans, J. A. Membrane Electroporation Theories: A Review. *Medical and Biological Engineering and Computing*. Springer-Verlag March 2, 2006, pp 5–14. https://doi.org/10.1007/s11517-005-0020-2.

(19) Qi, Y.; Ingólfsson, H. I.; Cheng, X.; Lee, J.; Marrink, S. J.; Im, W. CHARMM-GUI Martini Maker for Coarse-Grained Simulations with the Martini Force Field. *J. Chem. Theory Comput.* **2015**, *11* (9), 4486–4494. https://doi.org/10.1021/acs.jctc.5b00513.

(20) Jo, S.; Kim, T.; Iyer, V. G.; Im, W. CHARMM-GUI: A Web-Based Graphical User Interface for CHARMM. *J. Comput. Chem.* **2008**, *29* (11), 1859–1865.

https://doi.org/10.1002/jcc.20945.

(21) Klauda, J. B.; Venable, R. M.; Freites, J. A.; O'Connor, J. W.; Tobias, D. J.; Mondragon-Ramirez, C.; Vorobyov, I.; MacKerell, A. D.; Pastor, R. W. Update of the CHARMM All-Atom Additive Force Field for Lipids: Validation on Six Lipid Types. *J. Phys. Chem. B* **2010**, *114* (23), 7830–7843. https://doi.org/10.1021/jp101759q.

(22) Abraham, M. J.; Murtola, T.; Schulz, R.; Páll, S.; Smith, J. C.; Hess, B.; Lindah, E. Gromacs: High Performance Molecular Simulations through Multi-Level Parallelism from Laptops to Supercomputers. *SoftwareX* **2015**, *1–2*, 19–25. https://doi.org/10.1016/j.softx.2015.06.001.

(23) Fletcher, R.; Powell, M. J. D. A Rapidly Convergent Descent Method for Minimization. *Comput. J.* **1963**, *6* (2), 163–168. https://doi.org/10.1093/comjnl/6.2.163.

(24) Berendsen, H. J. C.; Postma, J. P. M.; Van Gunsteren, W. F.; Dinola, A.; Haak, J. R. Molecular Dynamics with Coupling to an External Bath. *J. Chem. Phys.* **1984**, *81* (8), 3684–3690. https://doi.org/10.1063/1.448118.

(25) Darden, T.; York, D.; Pedersen, L. Particle Mesh Ewald: An N ·log(N) Method for Ewald Sums in Large Systems. *J. Chem. Phys.* **1993**, *98* (12), 10089–10092. https://doi.org/10.1063/1.464397.

(26) Evans, D. J.; Holian, B. L. The Nose-Hoover Thermostat. *J. Chem. Phys.* **1985**, *83* (8), 4069–4074. https://doi.org/10.1063/1.449071.

(27) Parrinello, M.; Rahman, A. Polymorphic Transitions in Single Crystals: A New Molecular Dynamics Method. *J. Appl. Phys.* **1981**, *52* (12), 7182–7190. https://doi.org/10.1063/1.328693.

(28) Hess, B.; Bekker, H.; Berendsen, H. J. C.; Fraaije, J. G. E. M. LINCS: A Linear Constraint Solver for Molecular Simulations. *J. Comput. Chem.* **1997**, *18* (12), 1463–1472. https://doi.org/10.1002/(SICI)1096-987X(199709)18:12<1463::AID-JCC4>3.0.CO;2-H.

(29) Humphrey, W.; Dalke, A.; Schulten, K. VMD: Visual Molecular Dynamics. *J. Mol. Graph.* **1996**, *14* (1), 33–38. https://doi.org/10.1016/0263-7855(96)00018-5.

(30) Wassenaar, T. A.; Ingólfsson, H. I.; Böckmann, R. A.; Tieleman, D. P.; Marrink, S. J. Computational Lipidomics with Insane : A Versatile Tool for Generating Custom

Membranes for Molecular Simulations. *J. Chem. Theory Comput.* **2015**, *11* (5), 2144–2155. https://doi.org/10.1021/acs.jctc.5b00209.

(31) Bussi, G.; Donadio, D.; Parrinello, M. Canonical Sampling through Velocity Rescaling. *J. Chem. Phys.* **2007**, *126* (1), 014101. https://doi.org/10.1063/1.2408420.

(32) Fernández, M. L.; Risk, M.; Reigada, R.; Vernier, P. T. Size-Controlled Nanopores in Lipid Membranes with Stabilizing Electric Fields. *Biochem. Biophys. Res. Commun.* **2012**, *423* (2), 325–330. https://doi.org/10.1016/j.bbrc.2012.05.122.

(33) Tieleman, D. P. The Molecular Basis of Electroporation. *BMC Biochem.* **2004**, *5* (1), 1–12. https://doi.org/10.1186/1471-2091-5-10.

(34) Levine, Z. A.; Vernier, P. T. Life Cycle of an Electropore: Field-Dependent and Field-Independent Steps in Pore Creation and Annihilation. *J. Membr. Biol.* **2010**, *236* (1), 27–36. https://doi.org/10.1007/s00232-010-9277-y.

(35) Kirsch, S. A.; Böckmann, R. A. Membrane Pore Formation in Atomistic and Coarse-Grained Simulations. *Biochimica et Biophysica Acta - Biomembranes*. Elsevier October 1, 2016, pp 2266–2277. https://doi.org/10.1016/j.bbamem.2015.12.031.

(36) Tokman, M.; Lee, J. H. J.; Levine, Z. A.; Ho, M. C.; Colvin, M. E.; Vernier, P. T. Electric Field-Driven Water Dipoles: Nanoscale Architecture of Electroporation. *PLoS One* **2013**, *8* (4), e61111. https://doi.org/10.1371/journal.pone.0061111.

(37) Marrink, S. J.; de Vries, A. H.; Tieleman, D. P. Lipids on the Move: Simulations of Membrane Pores, Domains, Stalks and Curves. *Biochimica et Biophysica Acta - Biomembranes*. Elsevier January 1, 2009, pp 149–168. https://doi.org/10.1016/j.bbamem.2008.10.006.

(38) Bu, B.; Li, D.; Diao, J.; Ji, B. Mechanics of Water Pore Formation in Lipid Membrane under Electric Field. *Acta Mech. Sin. Xuebao* **2017**, *33* (2), 234–242. https://doi.org/10.1007/s10409-017-0635-1.

(39) Casciola, M.; Bonhenry, D.; Liberti, M.; Apollonio, F.; Tarek, M. A Molecular Dynamic Study of Cholesterol Rich Lipid Membranes: Comparison of Electroporation Protocols. *Bioelectrochemistry* **2014**, *100*, 11–17. https://doi.org/10.1016/j.bioelechem.2014.03.009.

(40) Laura Fernández, M.; Marshall, G.; Sagués, F.; Reigada, R. Structural and Kinetic Molecular Dynamics Study of Electroporation in Cholesterol-Containing Bilayers Supporting Information. *J. Phys. Chem. B* **2010**.

(41) Tarek, M. Membrane Electroporation: A Molecular Dynamics Simulation. *Biophys. J.* **2005**, *88* (6), 4045–4053. https://doi.org/10.1529/biophysj.104.050617.

(42) Vernier, P. T.; Levine, Z. A.; Ho, M. C.; Xiao, S.; Semenov, I.; Pakhomov, A. G. Picosecond and Terahertz Perturbation of Interfacial Water and Electropermeabilization of Biological Membranes. *J. Membr. Biol.* **2015**, *248* (5), 837–847. https://doi.org/10.1007/s00232-015-9788-7.

(43) Guidotti, G.; Brambilla, L.; Rossi, D. Cell-Penetrating Peptides: From Basic Research to Clinics. *Trends in Pharmacological Sciences*. April 2017, pp 406–424. https://doi.org/10.1016/j.tips.2017.01.003.

(44) Koren, E.; Torchilin, V. P. Cell-Penetrating Peptides: Breaking through to the Other Side. *Trends in Molecular Medicine*. Elsevier Current Trends July 1, 2012, pp 385–393. https://doi.org/10.1016/j.molmed.2012.04.012.

(45) Herce, H. D.; Garcia, A. E. Molecular Dynamics Simulations Suggest a Mechanism for Translocation of the HIV-1 TAT Peptide across Lipid Membranes. *Proc. Natl. Acad. Sci.* **2007**, *104* (52), 20805–20810. https://doi.org/10.1073/pnas.0706574105.

(46) Herce, H. D.; Garcia, A. E.; Litt, J.; Kane, R. S.; Martin, P.; Enrique, N.; Rebolledo, A.; Milesi, V. Arginine-Rich Peptides Destabilize the Plasma Membrane, Consistent with a Pore Formation Translocation Mechanism of Cell-Penetrating Peptides. *Biophys. J.* **2009**, *97* (7), 1917–1925. https://doi.org/10.1016/j.bpj.2009.05.066.

(47) Pamonsinlapatham, P.; Hadj-Slimane, R.; Lepelletier, Y.; Allain, B.; Toccafondi, M.; Garbay, C.; Raynaud, F. P120-Ras GTPase Activating Protein (RasGAP): A Multi-Interacting Protein in Downstream Signaling. *Biochimie* **2009**, *91* (3), 320–328. https://doi.org/10.1016/J.BIOCHI.2008.10.010.

(48) Tsoutsou, P.; Annibaldi, A.; Viertl, D.; Ollivier, J.; Buchegger, F.; Vozenin, M.-C.; Bourhis, J.; Widmann, C.; Matzinger, O. TAT-RasGAP $_{317–326}$ Enhances Radiosensitivity of Human Carcinoma Cell Lines *In Vitro* and *In Vivo* through Promotion of Delayed Mitotic Cell Death. *Radiat. Res.* **2017**, *187* (5), 562–569.

https://doi.org/10.1667/RR14509.1.

(49) Barras, D.; Lorusso, G.; Rüegg, C.; Widmann, C. Inhibition of Cell Migration and Invasion Mediated by the TAT-RasGAP317–326 Peptide Requires the DLC1 Tumor Suppressor. *Oncogene* **2014**, *33* (44), 5163–5172. https://doi.org/10.1038/onc.2013.465.

(50) Barras, D.; Lorusso, G.; Lhermitte, B.; Viertl, D.; Rüegg, C.; Widmann, C. Fragment N2, a Caspase-3-Generated RasGAP Fragment, Inhibits Breast Cancer Metastatic Progression. *Int. J. Cancer* **2014**, *135* (1), 242–247. https://doi.org/10.1002/ijc.28674.

(51) Michod, D.; Annibaldi, A.; Schaefer, S.; Dapples, C.; Rochat, B.; Widmann, C. Effect of RasGAP N2 Fragment–Derived Peptide on Tumor Growth in Mice. *JNCI J. Natl. Cancer Inst.* **2009**, *101* (11), 828–832. https://doi.org/10.1093/jnci/djp100.

(52) Pittet, O.; Petermann, D.; Michod, D.; Krueger, T.; Cheng, C.; Ris, H.-B.; Widmann, C. Effect of the TAT-RasGAP(317-326) Peptide on Apoptosis of Human Malignant Mesothelioma Cells and Fibroblasts Exposed to Meso-Tetra-Hydroxyphenyl-Chlorin and Light. *J. Photochem. Photobiol. B.* **2007**, *88* (1), 29–35. https://doi.org/10.1016/j.jphotobiol.2007.04.009.

(53) Heulot, M.; Chevalier, N.; Puyal, J.; Margue, C.; Michel, S.; Kreis, S.; Kulms, D.; Barras, D.; Nahimana, A.; Widmann, C. The TAT-RasGAP317-326 Anti-Cancer Peptide Can Kill in a Caspase-, Apoptosis-, and Necroptosis-Independent Manner. *Oncotarget* **2016**, *7* (39), 64342–64359. https://doi.org/10.18632/oncotarget.11841.

(54) Yang, M.; Brackenbury, W. J. Membrane Potential and Cancer Progression. *Frontiers in Physiology*. Frontiers July 17, 2013, p 185. https://doi.org/10.3389/fphys.2013.00185.

(55) Edwards, G.; Dora, K. A.; Gardener, M. J.; Garland, C. J.; Weston, A. H. K+ Is an Endothelium-Derived Hyperpolarizing Factor in Rat Arteries. *Nature* **1998**, *396* (6708), 269–272. https://doi.org/10.1038/24388.

(56) Knot, H. J.; Zimmermann, P. A.; Nelson, M. T. Extracellular K(+)-Induced Hyperpolarizations and Dilatations of Rat Coronary and Cerebral Arteries Involve Inward Rectifier K(+) Channels. *J. Physiol.* **1996**, *492 (Pt 2)* (Pt 2), 419–430.

(57) Klauschenz, E.; Scheller, A.; Wiesner, B.; Bienert, M.; Krause, E.; Oehlke, J.; Melzig, M.;

Beyermann, M. Cellular Uptake of an α-Helical Amphipathic Model Peptide with the Potential to Deliver Polar Compounds into the Cell Interior Non-Endocytically. *Biochim. Biophys. Acta - Biomembr.* **2002**, *1414* (1–2), 127–139. https://doi.org/10.1016/s0005-2736(98)00161-8.

(58) Derossi, D.; Joliot, A. H.; Chassaing, G.; Prochiantz, A. The Third Helix of the Antennapedia Homeodomain Translocates through Biological Membranes. *J. Biol. Chem.* **1994**, *269* (14), 10444–10450.

(59) Gao, C.; Mao, S.; Ditzel, H. J.; Farnaes, L.; Wirsching, P.; Lerner, R. A.; Janda, K. D. A Cell-Penetrating Peptide from a Novel PVII-PIX Phage-Displayed Random Peptide Library. *Bioorganic Med. Chem.* **2002**, *10* (12), 4057–4065. https://doi.org/10.1016/S0968-0896(02)00340-1.

(60) Futaki, S.; Suzuki, T.; Ohashi, W.; Yagami, T.; Tanaka, S.; Ueda, K.; Sugiura, Y. Arginine-Rich Peptides. An Abundant Source of Membrane-Permeable Peptides Having Potential as Carriers for Intracellular Protein Delivery. *J. Biol. Chem.* **2001**, *276* (8), 5836–5840. https://doi.org/10.1074/jbc.M007540200.

(61) Park, J.; Ryu, J.; Kim, K. A.; Lee, H. J.; Bahn, J. H.; Han, K.; Choi, E. Y.; Lee, K. S.; Kwon, H. Y.; Choi, S. Y. Mutational Analysis of a Human Immunodeficiency Virus Type 1 Tat Protein Transduction Domain Which Is Required for Delivery of an Exogenous Protein into Mammalian Cells. *J. Gen. Virol.* **2002**, *83* (5), 1173–1181. https://doi.org/10.1099/0022-1317-83-5-1173.

(62) Pooga, M.; Soomets, U.; Hällbrink, M.; Valkna, A.; Saar, K.; Rezaei, K.; Kahl, U.; Hao, J. X.; Xu, X. J.; Wiesenfeld-Hallin, Z.; et al. Cell Penetrating PNA Constructs Regulate Galanin Receptor Levels and Modify Pain Transmission in Vivo. *Nat. Biotechnol.* **1998**, *16* (9), 857–861. https://doi.org/10.1038/nbt0998-857.

(63) Leontiadou, H.; Mark, A. E.; Marrink, S. J. Molecular Dynamics Simulations of Hydrophilic Pores in Lipid Bilayers. *Biophys. J.* **2004**, *86* (4), 2156–2164. https://doi.org/10.1016/S0006-3495(04)74275-7.

(64) Gurtovenko, A. A.; Vattulainen, I. Ion Leakage through Transient Water Pores in Protein-Free Lipid Membranes Driven by Transmembrane Ionic Charge Imbalance. *Biophys. J.* **2007**, *92* (6), 1878–1890. https://doi.org/10.1529/biophysj.106.094797.

(65) Casciola, M.; Tarek, M. A Molecular Insight into the Electro-Transfer of Small Molecules through Electropores Driven by Electric Fields. *Biochim. Biophys. Acta - Biomembr.* **2016**, *1858* (10), 2278–2289. https://doi.org/10.1016/j.bbamem.2016.03.022.

(66) Gao, X.; Hong, S.; Liu, Z.; Yue, T.; Dobnikar, J.; Zhang, X. Membrane Potential Drives Direct Translocation of Cell-Penetrating Peptides. *Nanoscale* **2019**, No. January. https://doi.org/10.1039/C8NR10447F.

(67) Casciola, M.; Kasimova, M. A.; Rems, L.; Zullino, S.; Apollonio, F.; Tarek, M. Properties of Lipid Electropores I: Molecular Dynamics Simulations of Stabilized Pores by Constant Charge Imbalance. *Bioelectrochemistry* **2016**, *109*, 108–116. https://doi.org/10.1016/j.bioelechem.2016.01.006.

(68) Terrone, D.; Sang, S. L. W.; Roudaia, L.; Silvius, J. R. Penetratin and Related Cell-Penetrating Cationic Peptides Can Translocate Across Lipid Bilayers in the Presence of a Transbilayer Potential. *Biochemistry* **2003**, *42* (47), 13787–13799. https://doi.org/10.1021/bi035293y.

(69) Yesylevskyy, S.; Marrink, S. J.; Mark, A. E. Alternative Mechanisms for the Interaction of the Cell-Penetrating Peptides Penetratin and the TAT Peptide with Lipid Bilayers. *Biophys. J.* **2009**, *97* (1), 40–49. https://doi.org/10.1016/j.bpj.2009.03.059.

(70) Mueller, J.; Kretzschmar, I.; Volkmer, R.; Boisguerin, P. Comparison of Cellular Uptake Using 22 CPPs in 4 Different Cell Lines. *Bioconjug. Chem.* **2008**, *19* (12), 2363–2374. https://doi.org/10.1021/bc800194e.

(71) Takeuchi, T.; Futaki, S. Current Understanding of Direct Translocation of Arginine-Rich Cell-Penetrating Peptides and Its Internalization Mechanisms. *Chem. Pharm. Bull. Pharm. Bull.* **2016**, *64* (10), 1431–1437. https://doi.org/10.1248/cpb.c16-00505.

(72) Jiao, C.-Y.; Delaroche, D.; Burlina, F.; Alves, I. D.; Chassaing, G.; Sagan, S.; Internalization, P. Translocation and Endocytosis for Cell-Penetrating. *J. Biol. Chem.* **2009**, *284* (49), 33957–33965. https://doi.org/10.1074/jbc.M109.056309.

(73) Bechara, C.; Sagan, S. Cell-Penetrating Peptides: 20 Years Later, Where Do We Stand? *FEBS Letters*. No longer published by Elsevier June 19, 2013, pp 1693–1702. https://doi.org/10.1016/j.febslet.2013.04.031.

(74) Li, Z. L.; Ding, H. M.; Ma, Y. Q. Translocation of Polyarginines and Conjugated Nanoparticles across Asymmetric Membranes. *Soft Matter* **2013**, *9* (4), 1281–1286. https://doi.org/10.1039/c2sm26519b.

(75) Ackels, T.; Spehr, M.; Schiller, J.; Caillon, L.; Brock, R.; Olea, R. A.; Ulrich, A. S.; van Kuppevelt, T. H.; Klein, M. J.; Adjobo-Hermans, M. J. W.; et al. Membrane Permeation of Arginine-Rich Cell-Penetrating Peptides Independent of Transmembrane Potential as a Function of Lipid Composition and Membrane Fluidity. *J. Control. Release* **2017**, *256*, 68–78. https://doi.org/10.1016/j.jconrel.2017.04.013.

6 SUPPORTING INFORMATION

6.1 Chapter 3-SI

6.1.1 Bilayer area

The area on the xy plane is considered to define the pore formation time, which is the time at which a sudden increase in area happens. From SI-Figure 1 to SI-Figure 5 are plotted the bilayer areas for the different values of the field in the AA simulations. From SI-Figure 6 to SI-Figure 8 are plotted the bilayer areas for the different values of the field in the CG simulations. Each colour represents one of the five replicas.

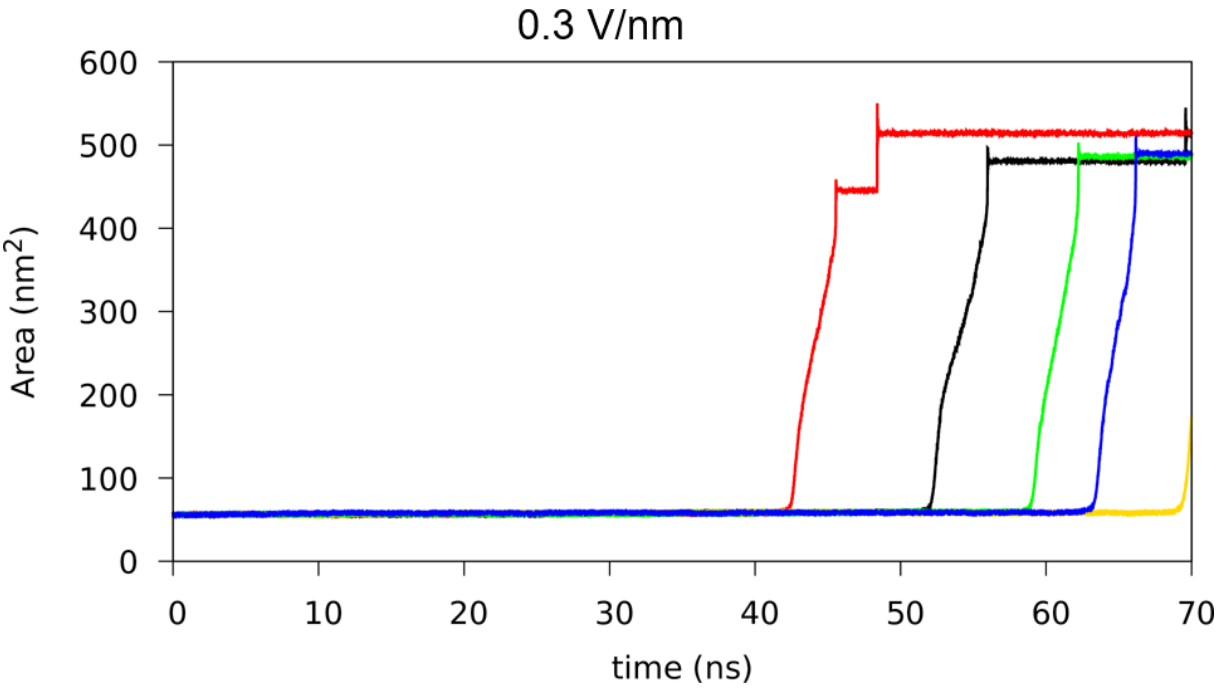

SI-Figure 1

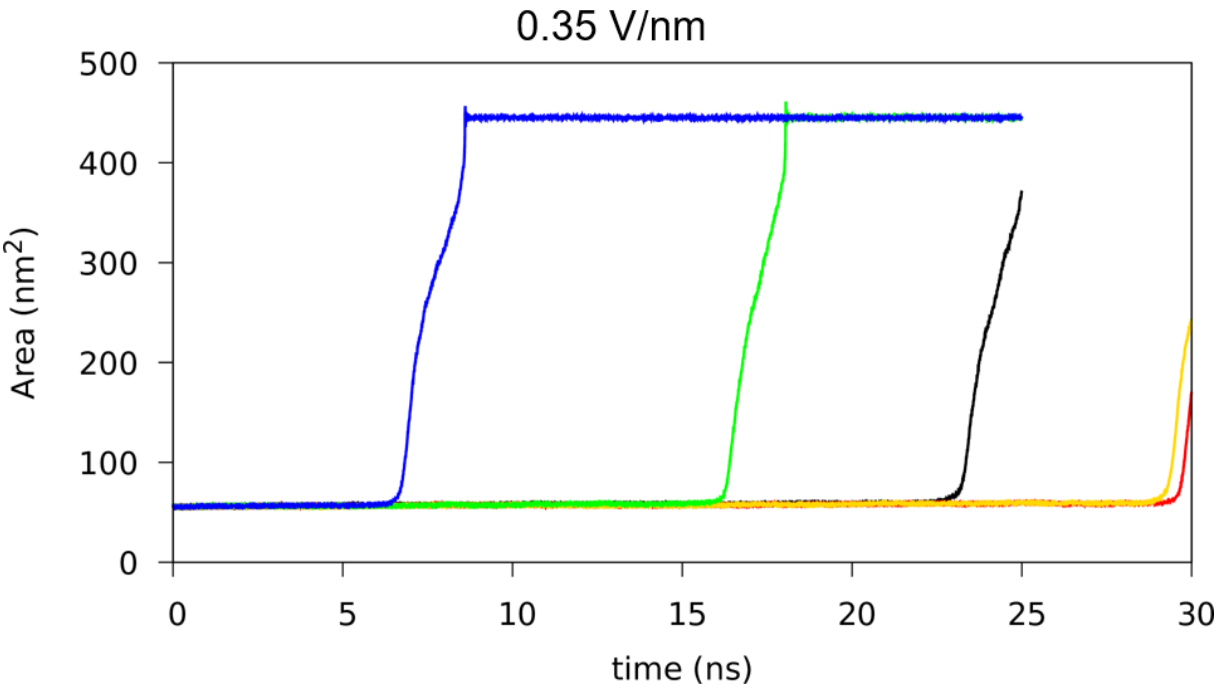

SI-Figure 2

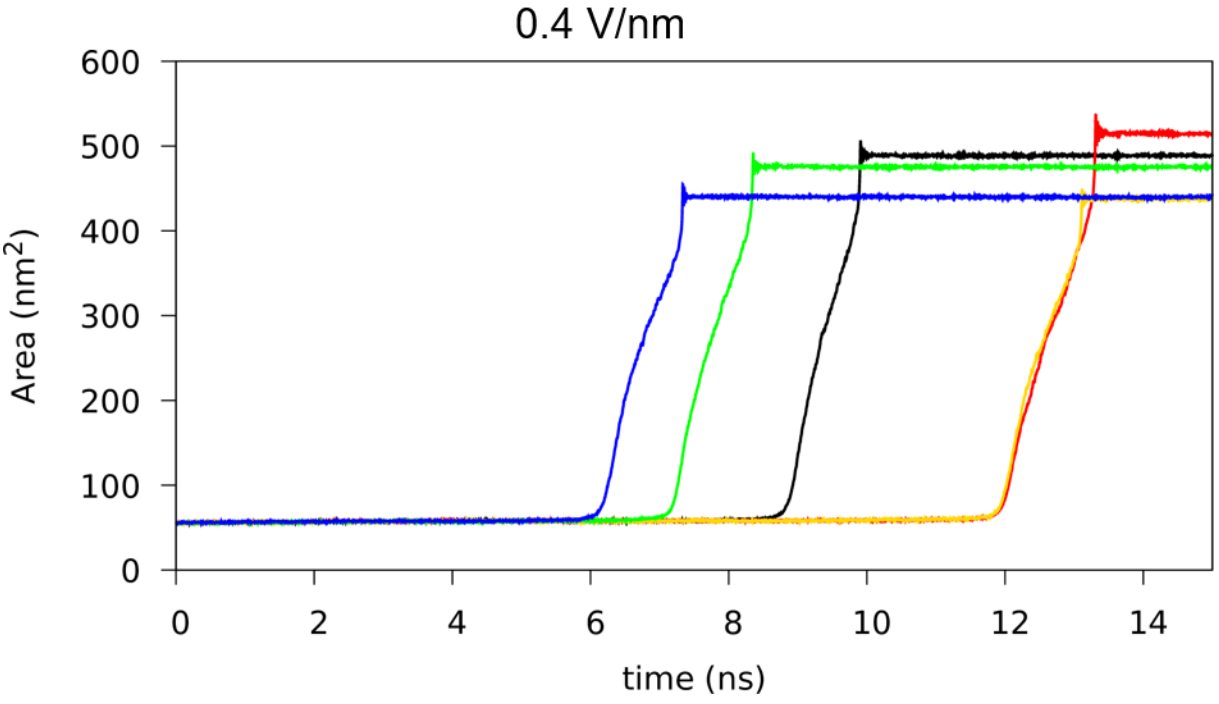

SI-Figure 3

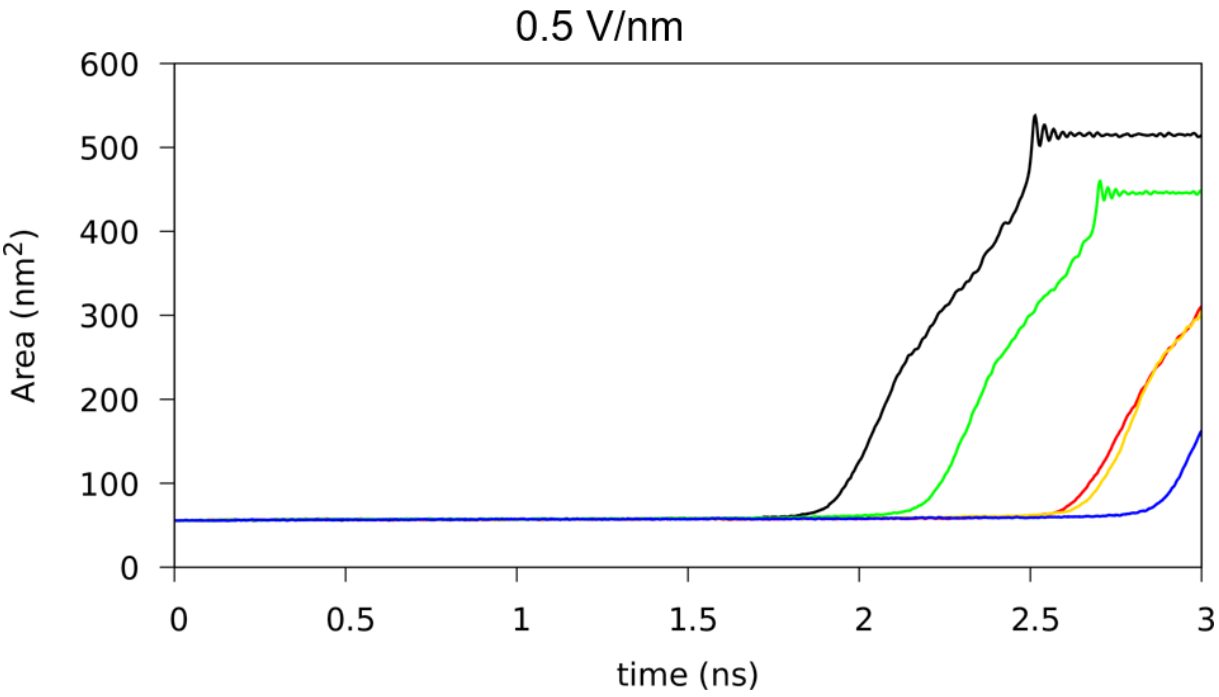

SI-Figure 4

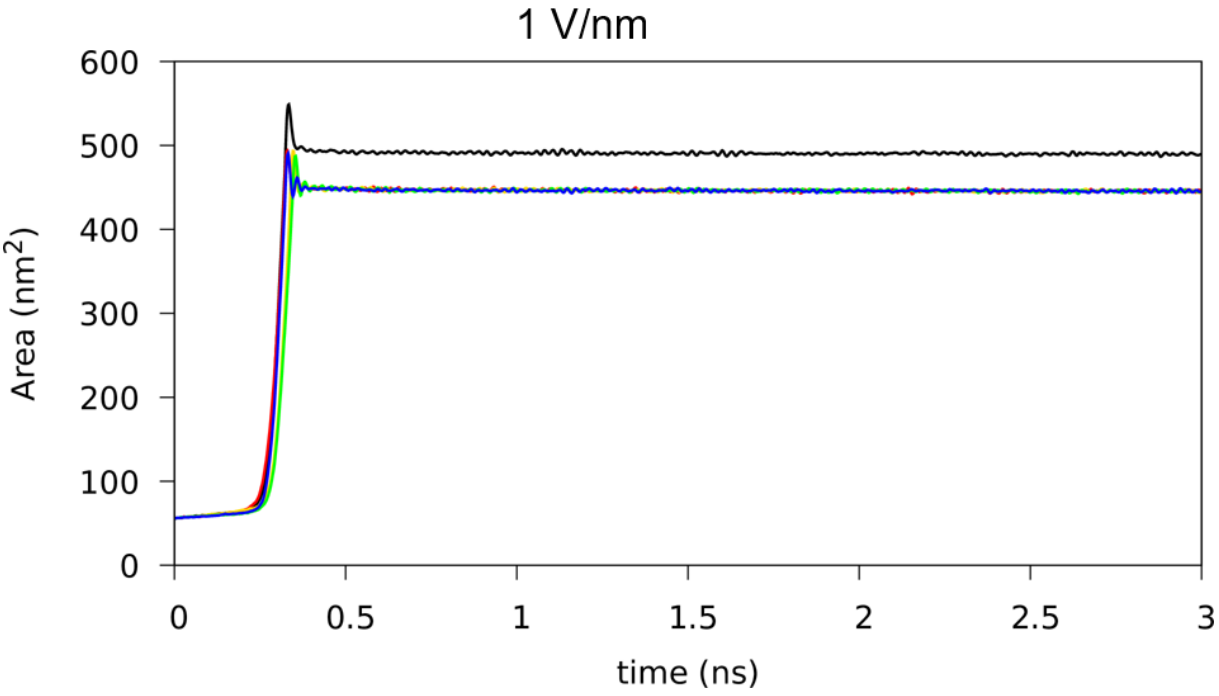

SI-Figure 5

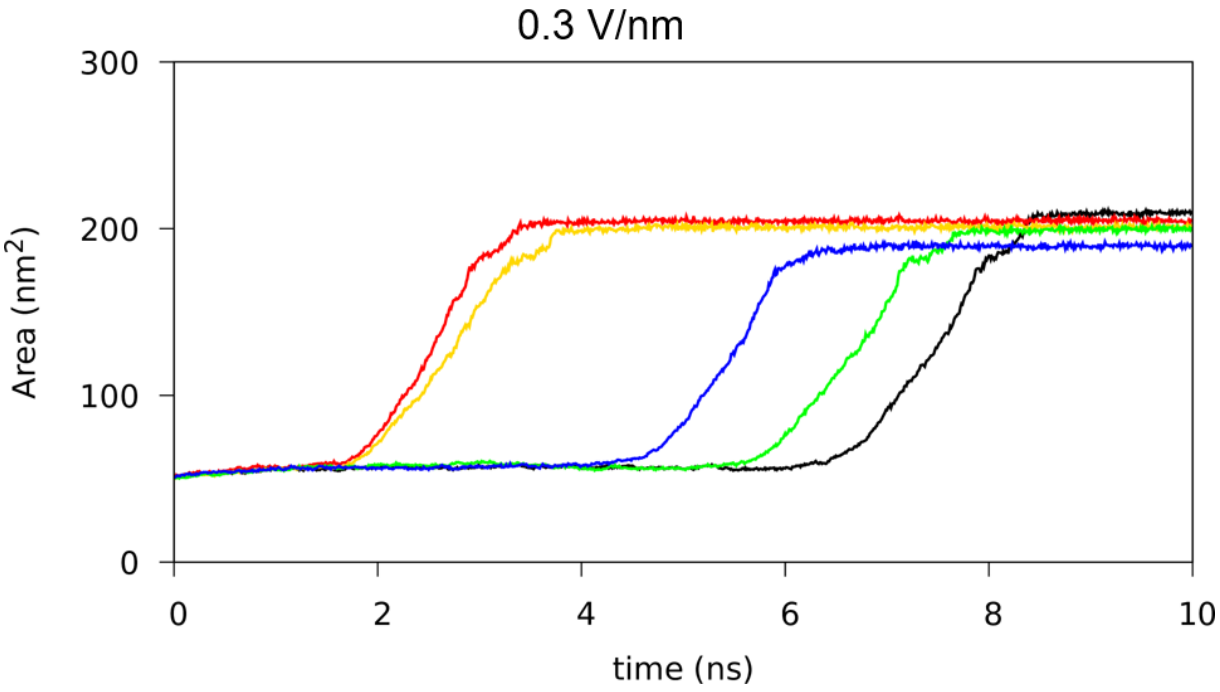

SI-Figure 6

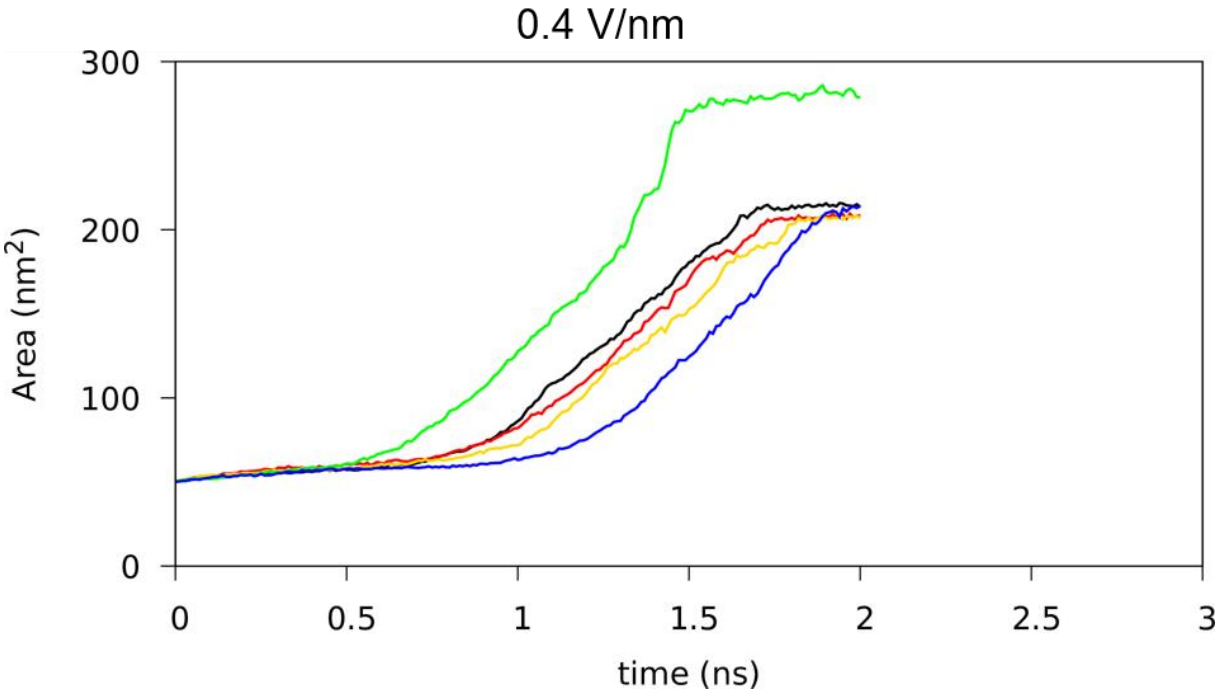

SI-Figure 7

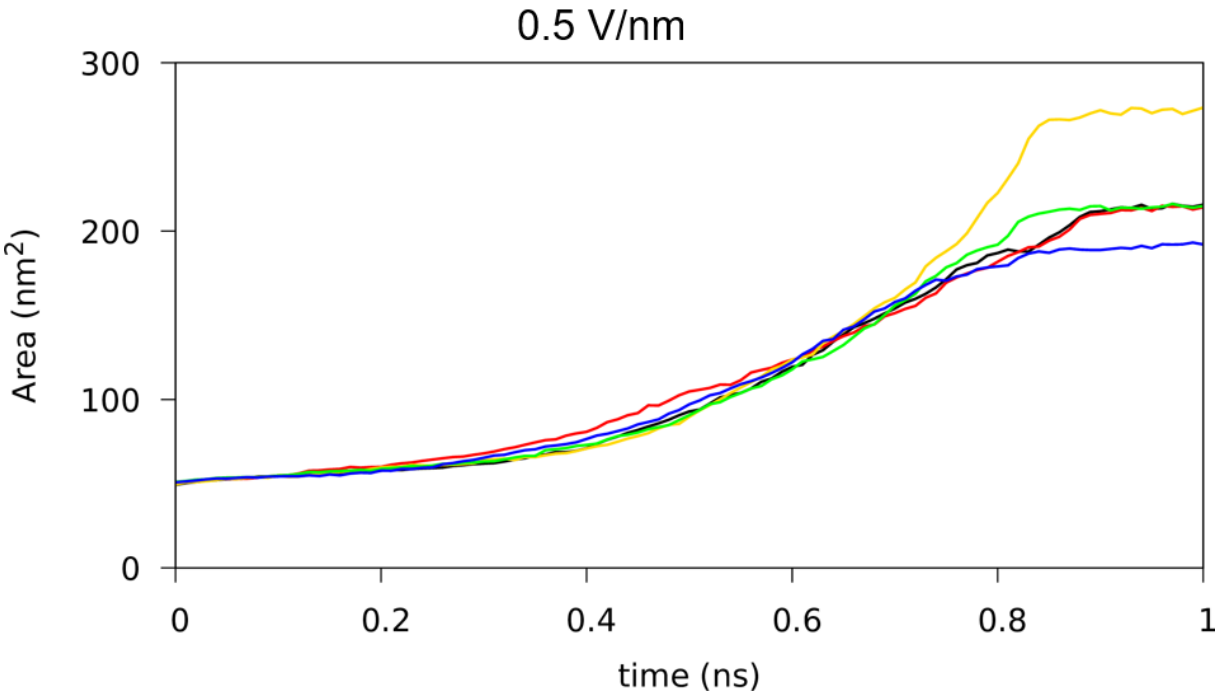

SI-Figure 8